JGR Solid Earth

RESEARCH ARTICLE
10.1029/2020JB019735

Key Points:
- Altimetry-predicted bathymetry uncertainties are modeled using multibeam bathymetry data
- A synthetic bathymetry sample generation method is proposed using a conditional random field, a Karhunen Loeve expansion, and a translation
- The uncertainty model shows that altimetry-predicted bathymetry is sufficiently accurate to estimate hazard from leading tsunami waves close to Chile

Supporting Information:
- Supporting Information S1

Correspondence to:
I. Sepúlveda,
sepulveda@ucsd.edu

Citation:
Sepúlveda, I., Tozer, B., Haase, J. S., Liu, P. L.-F., & Grigoriu, M. (2020). Modeling uncertainties of bathymetry predicted with satellite altimetry data and application to tsunami hazard assessments. *Journal of Geophysical Research: Solid Earth*, *125*, e2020JB019735. https://doi.org/10.1029/2020JB019735

Received 7 MAR 2020
Accepted 2 SEP 2020
Accepted article online 9 SEP 2020

Modeling Uncertainties of Bathymetry Predicted With Satellite Altimetry Data and Application to Tsunami Hazard Assessments

Ignacio Sepúlveda[1], Brook Tozer[1], Jennifer S. Haase[1], Philip L.-F. Liu[2,3,4], and Mircea Grigoriu[2]

[1]Institute of Geophysics and Planetary Physics, Scripps Institution of Oceanography, University of California San Diego, La Jolla, CA, USA, [2]Civil and Environmental Engineering, Cornell University, Ithaca, NY, USA, [3]Institute of Hydrological and Oceanic Sciences, National Central University, Jhongli, Taiwan, [4]Department of Civil and Environmental Engineering, National University of Singapore, Singapore

Abstract Models of bathymetry derived from satellite radar altimetry are essential for modeling many marine processes. They are affected by uncertainties which require quantification. We propose an uncertainty model that assumes errors are caused by the lack of high-wavenumber content within the altimetry data. The model is then applied to a tsunami hazard assessment. We build a bathymetry uncertainty model for northern Chile. Statistical properties of the altimetry-predicted bathymetry error are obtained using multibeam data. We find that a Von Karman correlation function and a Laplacian marginal distribution can be used to define an uncertainty model based on a random field. We also propose a method for generating synthetic bathymetry samples conditional to shipboard measurements. The method is further extended to account for interpolation uncertainties, when bathymetry data resolution is finer than ~10 km. We illustrate the usefulness of the method by quantifying the bathymetry-induced uncertainty of a tsunami hazard estimate. We demonstrate that tsunami leading wave predictions at middle/near field tide gauges and buoys are insensitive to bathymetry uncertainties in Chile. This result implies that tsunami early warning approaches can take full advantage of altimetry-predicted bathymetry in numerical simulations. Finally, we evaluate the feasibility of modeling uncertainties in regions without multibeam data by assessing the bathymetry error statistics of 15 globally distributed regions. We find that a general Von Karman correlation and a Laplacian marginal distribution can serve as a first-order approximation. The standard deviation of the uncertainty random field model varies regionally and is estimated from a proposed scaling law.

1. Introduction

Many geophysical processes in marine environments are influenced by seafloor bathymetry. Some examples are ocean tides (Egbert & Ray, 2001), tsunamis (Mofjeld et al., 2001), ocean circulation (Gille et al., 2004), internal waves (Hu et al., 2020), and turbulent mixing (Kunze & Smith, 2004). The propagation of ocean surface waves is strongly affected by bathymetry when depths are comparable to their wavelengths. Tsunami waves, in particular, are affected by bathymetry at all ocean depths. High-resolution bathymetry data, such as those obtained from shipboard multibeam surveys, however, are very scarce. A recent compilation of publicly available shipboard bathymetry data found that only 11% of the seafloor has been surveyed at 15 arcsec (Tozer et al., 2019). For the remaining areas, indirect approaches have been adopted to fill the voids. A great advance was made in the prediction of bathymetry with the advent of satellite altimetry (e.g., Smith & Sandwell, 1994, 1997). The prediction of bathymetry by means of satellite altimetry is limited to wavelengths larger than ~10 km (Tozer et al., 2019). Thus, the altimetry-predicted bathymetry contains errors at short wavelengths. Several digital elevation models (DEM herein) based on satellite altimetry data have been produced over the last three decades (e.g., Becker et al., 2009; Smith & Sandwell, 1997; Tozer et al., 2019; Weatherall et al., 2015), and they are massively exploited in ocean engineering, geophysical/oceanographic research, and education. The bathymetry obtained from DEMs is usually interpolated to estimate the bathymetry at a desired point location (e.g., at the nodes of a regular grid). This interpolation produces errors for length scales smaller than the data resolution. Little attention has been paid to the

uncertainties of the altimetry-predicted bathymetry and interpolations or how they propagate into derived results. These uncertainties are the focus of this paper.

Higher resolution measurements (i.e., from shipboard methods) are required to quantify errors in predicted bathymetry. When errors are statistically described, however, stochastic approaches can be used to model their uncertainty. Many studies have demonstrated that the topography and bathymetry of the Earth exhibit a general fractal behavior at wavenumbers greater than $\sim 0.01\,\mathrm{km}^{-1}$ (i.e., wavelengths $\lambda < 100\,\mathrm{km}$), with unknown maximum wavenumber (e.g., Bell, 1975; Mandelbrot, 1967). The relevant consequence of this fractal behavior (also known as self-similarity) is that the power spectral density of topo-bathymetry is characterized by a function which follows a constant power law decay for high wavenumbers. This distinctive power spectral density is then employed to determine an autocorrelation function. While the distribution of the high wavenumber content of the bathymetry (i.e., marginal distribution) was first modeled as Gaussian, it was soon demonstrated that distributions are non-Gaussian (Goff, 1991). Indeed, Smith and Sandwell (1994) and recently Tozer et al. (2019) showed that errors in their predicted bathymetry model, which are predominantly caused by the absence of certain high wavenumber content, exhibit a non-Gaussian distribution in many locations, with longer tails and a higher peak than a Gaussian distribution.

Previous studies have used the statistical properties of the bathymetry and stochastic approaches to generate random realizations of regional (synthetic) bathymetry samples for wavelengths $\lambda < 100\,\mathrm{km}$. Goff and Jordan (1988), in particular, proposed key elements to create synthetic bathymetry of abyssal hills, and several follow-up studies proposed better non-Gaussian random field models for length scales of 2–10 km (e.g., Goff, 1993, 2010; Goff & Arbic, 2010). Williams et al. (2017) also used a stochastic approach to generate synthetic bathymetry samples of fjords of Greenland in their ice-sea interaction studies. A valuable application of generating synthetic samples of high wavenumber content is to determine the impact of bathymetry uncertainties in oceanographic and geophysical modeling. A Monte Carlo simulation using a tsunami propagation model, for instance, can be adopted to determine the statistics of the tsunami response uncertainty due to the uncertain bathymetry.

This paper proposes a methodology to quantify the uncertainties of altimetry-predicted bathymetry and its impact on tsunami responses in northern Chile. In section 2, we analyze the main source of altimetry-predicted bathymetry errors. In section 3, we determine the bathymetry error statistics in northern Chile, and we use them to define the second moment properties for an uncertainty model. This uncertainty model is then employed to generate synthetic bathymetry samples with a new proposed method. In section 4, we quantify the uncertainty of tsunami responses due to altimetry-predicted bathymetry errors via a Monte Carlo simulation that uses the bathymetry samples. In section 5, we further analyze the statistical properties of altimetry-predicted bathymetry errors in 15 multibeam surveyed regions around the world, aiming to define a first-order approximation uncertainty model that can be used globally.

2. Errors in Altimetry-Predicted Bathymetry

The gradient of the altimetry data is the main constraint in the technique for predicting bathymetry. Its errors are summarized below. The hydrostatic response of the ocean causes its surface to closely follow the surface of constant gravitational potential energy called the geoid. Because bathymetry causes gravity anomalies large enough to be recorded at the sea surface, in principle the bathymetry can be derived from the gradient in the ocean surface height measured by highly accurate satellite altimetry (Smith, 1998; Smith & Sandwell, 1994). However, satellite altimetry data can only predict the bathymetry at wavelengths between ~160 and ~10 km. The upper bound of ~160 km occurs because isostatic compensation of features with larger wavelengths dampens their gravity anomalies (Smith & Sandwell, 1994). The lower wavelength bound of ~10 km occurs because at the ocean surface, the upward continuation attenuates high wavenumber gravity anomalies generated at the seafloor (Blakely, 1996), reducing their amplitude below the satellite altimetry noise level. Sparse shipboard soundings are interpolated to recover variations with wavelengths >160 km. However, there are no means to recover information associated with the high wavenumber content. Assuming a linear relation between gravity anomalies and bathymetry, we can determine the bathymetry between wavelengths of ~160 and ~10 km. The Inverse Nettleton procedure (Smith & Sandwell, 1994) uses a linear regression to relate band-pass filtered shipboard bathymetry measurements to altimetry-predicted gravity anomalies. Figures 1 and 2 show the altimetry-predicted bathymetry, $\tilde{h}$ (top panels), in two areas in

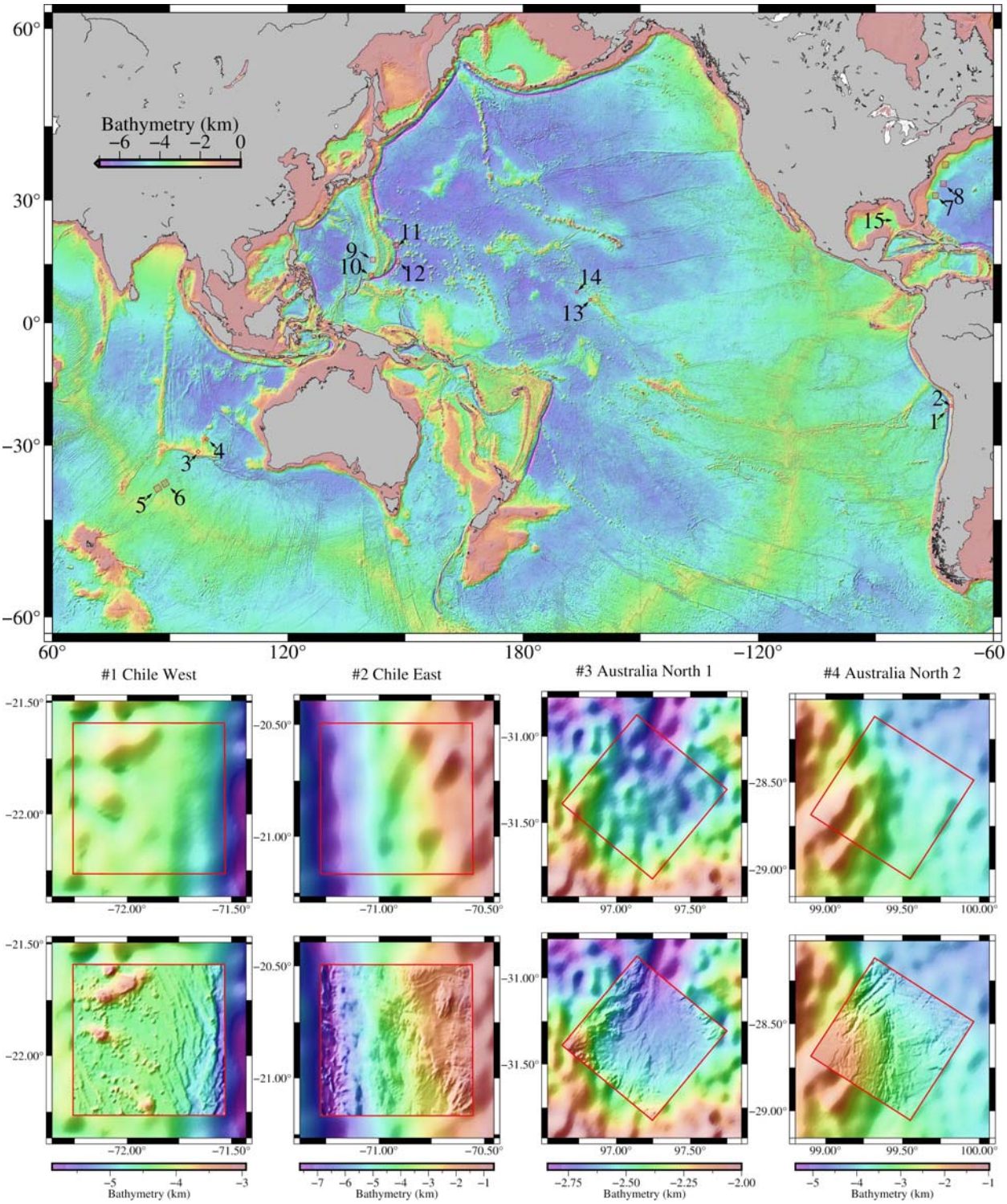

Figure 1. Top panel: Global map indicating the locations of the 15 multibeam surveys used in this study. Lower panels: Comparison between the altimetry-predicted bathymetry, $\tilde{h}$ (first row), and the multibeam bathymetry, h (second row), for Surveys #1 to #4. The labels indicate the corresponding number in the reference map and the name of the region. The red squares enclose the multibeam survey areas, whose dimensions vary according to the available multibeam data, between $75 \times 75\ km^2$ (Regions #1 to #4 and #13 to #15) and $140 \times 140\ km^2$ (Regions #5 to #12).

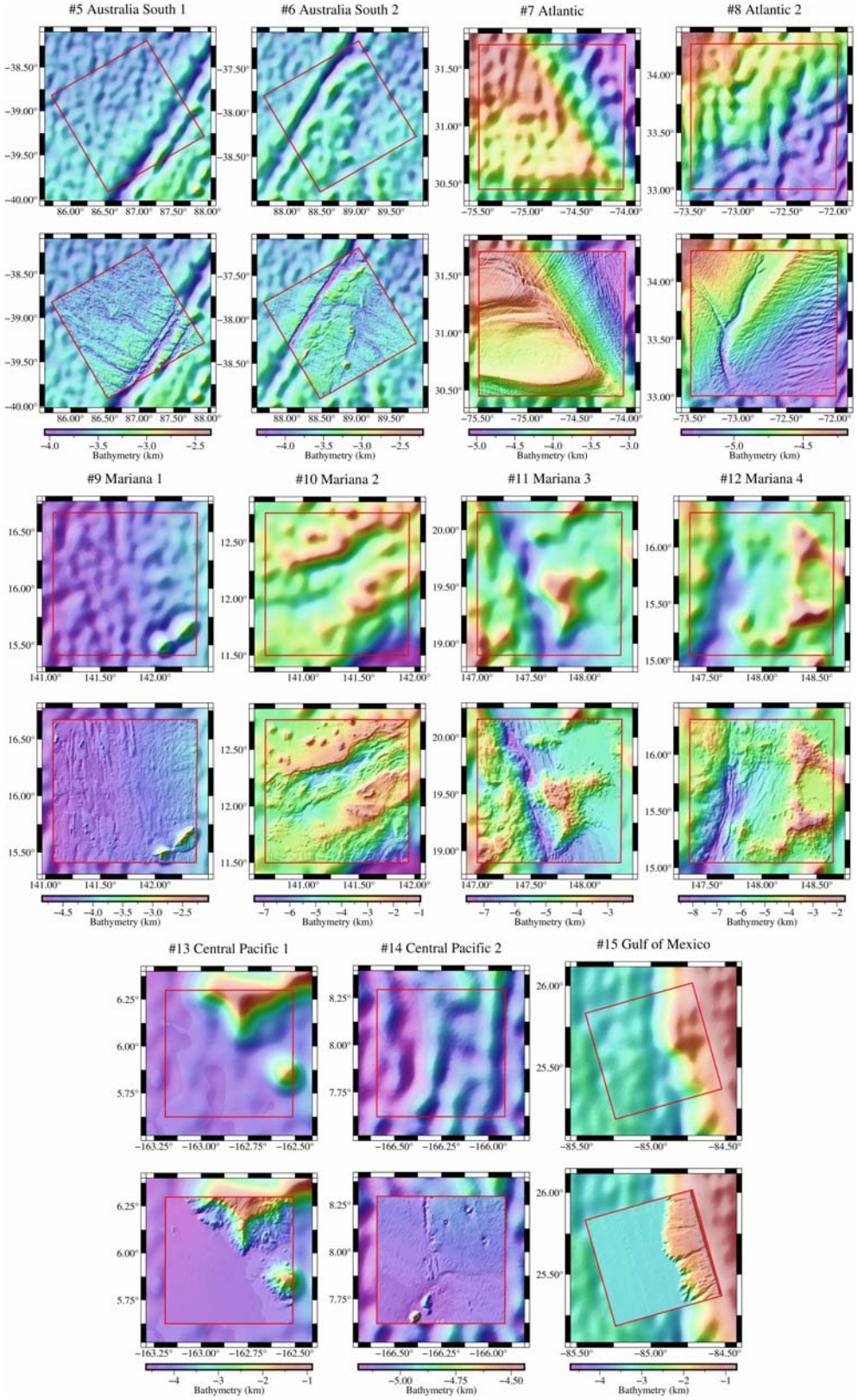

Figure 2. Comparison between the altimetry-predicted bathymetry and multibeam bathymetry for Surveys #5 to #15. Explanation as in Figure 1.

northern Chile (Samples #1 and #2) and 13 additional areas near the southwestern coast of Australia (Samples #3 to #6), the East Coast of the United States (Samples #7 and #8), near the Mariana Islands (Samples #9 to #12), Central Pacific (Samples #13 and #14), and the Gulf of Mexico (Sample #15), obtained from the SRTM15+V2.0 DEM. The samples are extracted from a grid containing altimetry predictions only (i.e., not containing shipboard soundings).

In recent years, high-resolution multibeam surveys that span large areal extents ($>75\times75$ km^2) have become publicly available. These data make it possible to describe the statistical properties of the bathymetry over a broad range of wavenumbers. Bathymetry information obtained with multibeam technology has high accuracy at a horizontal resolution of roughly 7% of the mean water depth (Mayer et al., 2018). This is significantly better than the altimetry-predicted bathymetry, and it can be considered a reference for the true bathymetry, defined in this study as h. Hence, we can use multibeam data to quantify errors of the altimetry-predicted bathymetry. Figures 1 and 2 show multibeam surveys conducted by Geomar (Geersen et al., 2018; Kopp et al., 2016) in northern Chile, by Geoscience Australia in Australia, and by the Center for Coastal and Ocean Mapping of the University of New Hampshire in the remaining regions. All surveys cover at least 75×75 km^2, with horizontal resolution finer than 500 m (i.e., with survey depths shallower than 7 km). The predicted bathymetry, $\tilde{h}$, is noticeably smoother than h (lower panels), due to the lack of high-wavenumber content in the altimetry-predicted bathymetry.

In the next section, we will quantitatively describe the altimetry-predicted bathymetry errors in northern Chile, where bathymetry has been comprehensively surveyed by Geomar, as an example to demonstrate how the bathymetry uncertainty model has been defined. This area is also susceptible to the occurrence of tsunamis and so serves as a good test case for examining the impact of the bathymetry errors on tsunami hazard simulations. At the end of the manuscript, we describe altimetry-predicted bathymetry error statistics for the other regions shown in Figures 1 and 2 suggest a general relation for bathymetry errors.

3. Uncertainty Model for Altimetry-Predicted Bathymetry in Chile

3.1. Statistical Analysis of Bathymetry

Before assessing the altimetry-predicted bathymetry errors, we shall first gain more insight into the statistical properties of the true bathymetry, h, represented by the multibeam surveys #1 and #2 in Figure 1. First, we compute the power spectral densities of the Chilean multibeam surveys, which are useful to assess the bathymetry at different length scales. We use a discrete Fourier transform (DFT). The data are interpolated to a regular grid, as required by the DFT, at a resolution of 500 m, which is equal or coarser than the effective data resolution of the bathymetric sample regions. The power spectral density is calculated by computing the Fourier transform of the bathymetry and by squaring the amplitude of each wavenumber bin. To compute the discrete Fourier transform, we use the fast Fourier transform algorithm implemented in Matlab (function **FFT2**). The power spectral amplitudes are normalized by $P = P'\Delta^2/N_n$, where P' is the nonnormalized power spectral density (i.e., output from **FFT2**), Δ is the separation between grid nodes (i.e., 500 m), and N_n is the number of grid nodes in the regions. By adopting this normalization, the following relation holds:

$$\sigma^2 = \sum_{i=1}^{N_x}\sum_{j=1}^{N_y}\frac{1}{\Delta^2 N_n}P(k_{xi},k_{yj}), \tag{1}$$

where σ^2 is the spatial variance of the bathymetry, (i,j) represents a wavenumber bin, N_x and N_y are the number of nodes in the local coordinate axes (i.e., $N_x\times N_y = N_n$), and k_{xi} and k_{yj} are wavenumbers with the unit of m^{-1}. The amplitudes of the power spectral density of a two-dimensional field have the unit of m^4. Edge effects are minimized by detrending the bathymetry, using a least-squares fit, and tapering the boundaries of the regions using a sinusoidal tapering window function, W_f, which multiplies the water depths of the grid nodes. The window function has the form

$$W_f(d_b) = \begin{cases} 0.5(1-\cos(\pi d_b/w_l)), & \text{for } d_b < w_l, \\ 1, & \text{for } d_b \geq w_l, \end{cases} \tag{2}$$

where d_b is the distance from a grid node to the boundary of the regions and w_l is the window width. Setting $w_l = 5$ km is sufficient to avoid artifacts at $k_x = 0$ and $k_y = 0$. We also split the bathymetry data into four subsamples and compute the average of the resulting power spectral densities to reduce numerical spectral

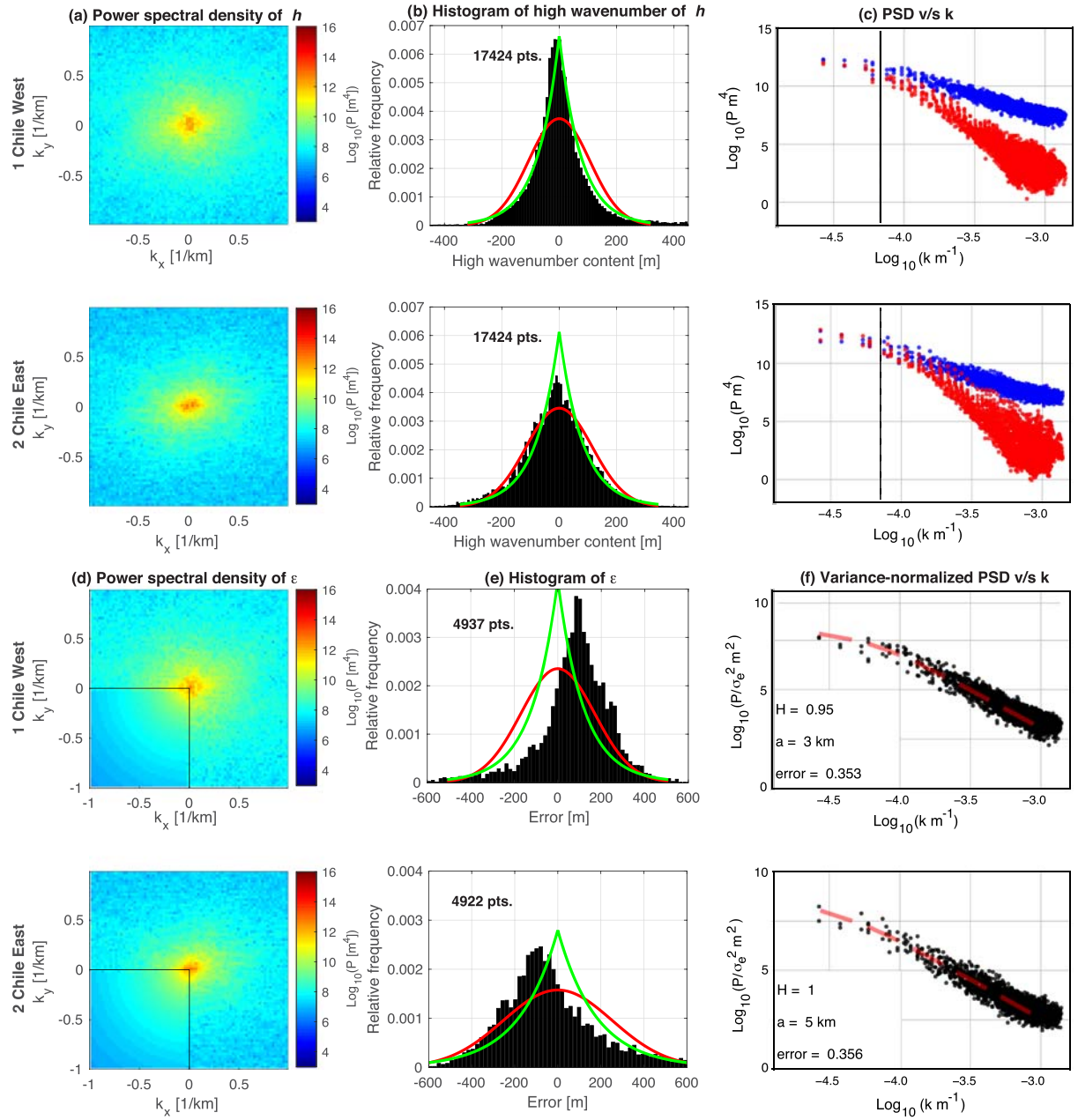

Figure 3. (a) Power spectral densities of the two multibeam surveys in Chile shown in Figure 1. (b) Black bars represent the histograms of the high wavenumber content of the multibeam bathymetry, isolated using Equation 3. A total of 17,424 points are used in the histograms. Green and red lines represent the best fit Laplacian and Gaussian distributions, respectively, with zero mean and equivalent variance. (c) Blue dots represent the power spectral density of the multibeam data h collapsed in terms of k (same as panel (a)). Red dots represent the power spectral density of $\bar{h}$. The black vertical lines indicate $W_L = 0.5$. (d) Power spectral densities (i.e., Fourier transform of $c(\xi)$) of ϵ. The lower left corner shows the modeled power spectral density for a Von Karman function with $a = 4$ km, $H = 0.975$, and $\sigma_e = 160$ m. (e) Histograms of ϵ (black bars), modeled Laplacian distribution (green line), and modeled Gaussian distribution (red line) using the same sample variance. (f) Variance-normalized power spectral density of ϵ as a function of k. The dashed red curves correspond to the best fit Von-Karman curve. Values of the best fit values of H, a, and rms error on a logarithmic scale are reported in the insets.

noise. The spectra of h of #1 and #2 in Figure 1 are shown in Figure 3a. The two-dimensional power spectral densities of the Chilean surveys have higher power at low wavenumbers and are approximately isotropic. For isotropic regions, the power spectra can be modeled as a function of the wavenumber only. Figure 3c shows the same power spectral densities as Figure 3a, collapsed to one dimension as a function of $k = \sqrt{k_x^2 + k_y^2}$ (blue dots). The blue dots show little dispersion, indicating that the isotropic assumption is adequate for the analyzed multibeam samples. Another relevant characteristic is that the spectral decay has a nearly

constant negative slope for high wavenumbers. Hence, the samples exhibit a fractal (self-similar) behavior, which extends to wavenumbers of $k = 10^{-3}$ m^{-1} (i.e., wavelengths $\lambda = 1$ km). The adequacy of the isotropic assumption and the fractal behavior observed in northern Chile are analyzed later for the other regions.

Another relevant statistical property of the bathymetry is the marginal distribution (or 1-point statistics), which we equate to the spatial histogram of h in this study. The bathymetry histograms are very different between the two Chilean samples when all length scales are considered. They have different spatial trends and average values. However, after removing low wavenumber content using the low-pass filter of Smith and Sandwell (1994),

$$W_L(k, \bar{h}) = \left(1 + Ak^4 e^{4\pi k|\bar{h}|}\right)^{-1}, \tag{3}$$

where k is the wavenumber in km^{-1}, $\bar{h}$ is the depth reference (e.g., here we use the mean value, in kilometers) and A is an empirical dimensional parameter defining the filtered wavenumbers, we observe that the high wavenumber content of the bathymetry exhibits the same histogram distribution for both regions. The black bars in Figure 3b present such histograms. We adopt this low-pass filter because it is also used by Tozer et al. (2019) to remove high wavenumber noise created by upward continuation and the noise in the altimetric gravity data, when creating the SRTM15+V2.0 DEM model. We apply this as a high-pass filter to the multibeam data (i.e., the reference for the true bathymetry) to produce the high wavenumber content, which is missing in the altimetry predicted bathymetry of SRTM15+V2.0 DEM. We use $A = 1{,}200$ km^4 (Tozer et al., 2019), which corresponds to a wavenumber cut-off of roughly 10^{-1} km^{-1} for shallow areas (i.e., wavelengths of ~10 km at 2.5 km depths). Some variations are observed in the filtered wavelengths for different regions because the filter (and the upward continuation phenomenon) depends on the reference depth. Further analysis of the relation between the parameter A, the reference depth, and the filtered wavenumbers are given in the supporting information. Figure 3b shows Laplacian and Gaussian distribution functions scaled with the high wavenumber content variance (i.e., same variance as black histograms). The histograms show long tails and a sharp peak at zero. The histograms of both Chilean regions are better fit by the Laplacian rather than a Gaussian function. This is a relevant characteristic because it shows that high wavenumber content, which is absent in altimetry-predicted bathymetry and which is expected to be the main cause of DEM errors, can be modeled with a Laplacian marginal distribution.

The red dots in Figure 3c show the collapsed spectra of the altimetry predicted bathymetry, $\tilde{h}$, in terms of $k = \sqrt{k_x^2 + k_y^2}$. The black vertical lines in the panels indicate the wavenumber at which W_L of Equation 3 becomes 0.5, indicating the wavenumber from which altimetry does not predict the bathymetry. To the left of the line at $W_L = 0.5$, the spectra of h and $\tilde{h}$ yield similar amplitudes. To the right of $W_L = 0.5$, conversely, the amplitudes of $\tilde{h}$ are much smaller than the the amplitudes of h, as expected. This provides the rationale for the statistical behavior of the altimetry-predicted bathymetry errors. Next, we shall deduce the empirical statistics of these errors, defined as

$$\epsilon = \tilde{h} - h. \tag{4}$$

3.2. Statistical Model for the Altimetry-Predicted Bathymetry Errors (ϵ)

We determine the second moment properties of ϵ in Regions #1 and #2 in northern Chile by computing the autocorrelation coefficient function and the histogram.

3.2.1. Autocorrelation Coefficient Function for the Altimetry-Predicted Bathymetry Errors (ϵ)

The black dots of Figure 3f represent the variance-normalized power spectral densities of ϵ. We present the variance-normalized spectra and analyze the spectral shape and the variance separately. The power spectral densities presented in Figure 3a are equivalent to the Fourier transform of the autocovariance defined as $c(\xi) = E[(h_{(x)} - \bar{h})(h_{(x+\xi)} - \bar{h})]$. The variance-normalized power spectral density, on the other hand, corresponds to the Fourier transform of the autocorrelation coefficient function, defined as $r(\xi) = E[(\epsilon_{(x)} - \bar{\epsilon})(\epsilon_{(x+\xi)} - \bar{\epsilon})]/\sigma_\epsilon^2$ (Grigoriu, 2012). Here, $E()$ is the expectation operator, σ_ϵ^2 is the total sample variance of ϵ, and $\bar{\epsilon}$ is the mean error. To remove numerical artifacts, each region is split into four subregions and multiplied by a 5 km taper. We do not detrend the variance normalized power spectral densities of ϵ because errors are expected to correspond to high wavenumbers.

The spectra in Figure 3f (black dots) show little dispersion, which indicates that isotropy is a simple and reasonable assumption for ϵ in the Chilean regions. The power spectral densities have an approximately

constant power law decay at high wavenumbers and a plateau at low wavenumbers. We model the power spectral densities using a Von Karman function (Goff & Jordan, 1988) with the form

$$P(k_x, k_y) = \frac{4\pi\sigma_e^2 H a_x a_y}{(1 + a_x^2 k'^2_x + a_y^2 k'^2_y)^{1+H}}. \quad (5)$$

The Von Karman covariance function, used later to build random field models, has the form

$$c(\xi) = \sigma_e^2 \frac{2^{1-H}}{\Gamma(H)} \bar{d}_\xi^H K_H(\bar{d}_\xi),$$
$$\bar{d}_\xi = \sqrt{\frac{(\xi_x)^2}{a_x^2} - \frac{(\xi_y)^2}{a_y^2}} > 0. \quad (6)$$

In these equations, $\Gamma(H)$ is the Gamma function, K_H is the modified Bessel function of the second kind of order H, $\xi = (\xi_x, \xi_y)$ is the distance between neighbor locations, and kx' and ky' are wavenumbers with units of radians per meter. Four shape parameters have to be specified in the Von Karman function. The shape parameter H is known as the Hurst number, and it controls the power law decay at high wavenumbers. As seen in Equation 5, the power law decay at high wavenumber is proportional to $k^{-(2+2H)}$. The parameters a_x and a_y are the characteristic correlation lengths of the bathymetry along the easting and northing directions, respectively. Because we assume that ϵ is isotropic, $a_x = a_y = a$. Shorter values of a_x and a_y extend the plateau region and move the power law decay region of the function to higher wavenumbers. The total variance σ_e^2 constitutes a shape parameter which controls the amplitude of the power spectral density. Because σ_e^2 is equal to the integral of the power spectral density over all wavenumbers, σ_e^2 increases with increasing spectral amplitudes. The correlation coefficient function model $r(\xi)$ is given by $r(\xi) = c(\xi)/\sigma_e^2$. The shape parameters H and a are calibrated using the variance-normalized power spectral densities of Figure 3f. The red dashed curves in Figure 3f represent the Von Karman function with the best least squares fit to each local spectra. The values of a and H and the fitting errors (in logarithmic units) are shown for each spectra. The average Hurst number for the two regions is $H = 0.975$, which has a power law decay of -3.95 at high wavenumbers. The average correlation length a is 4 km. The covariance model is defined by specifying a variance, σ_e^2. Both bathymetry samples in Chile have a value of σ_e close to 160 m. Figure 3d shows the two-dimensional power spectral densities of ϵ, which correspond to the Fourier transform of the autocovariance. The proposed model for the Chilean samples of ϵ is presented in the bottom left corner, using the Von Karman autocovariance function with the average parameters of $a = 4$ km, $H = 0.975$, and $\sigma_e = 160$ m. We observe that both samples of ϵ are reasonably well represented by the proposed power spectral density model.

3.2.2. Histograms of the Altimetry-Predicted Bathymetry Errors (ϵ)

Figure 3e shows the histograms of the altimetry-predicted bathymetry errors, ϵ, for the two regions studied in Chile. While the histograms present some deviation from zero mean, their shape is closer to a Laplacian distribution than a Gaussian. This can be expected when the source of error is due only to the lack of high wavenumber content in the model bathymetry. Therefore, in the next section, we use the Laplacian distribution and the modeled Von Karman autocovariance function to propose a bathymetry uncertainty model based on a random field model. The spatial histogram and autocovariance of the bathymetry values in each region yield the marginal distribution and covariance of the random field, respectively, when probability properties are ergodic and when sample sizes (i.e., >75 km) are much larger than correlation lengths (i.e., $a = 4$ km). While the second condition is fulfilled, the ergodicity condition is more difficult to validate. Based on the similarities of statistics between the two Chilean regions, though, we conclude that ergodicity holds in the study area in northern Chile. The assumptions of isotropy and ergodicity, which are somewhat supported by the multibeam data analysis of Figure 3, will be further discussed in section 5 for every region of Figures 1 and 2. Finally, we assume that the constant spectral decay extends to wavelengths as short as $\lambda = 100$ m. This assumption means that the fractal behavior is extended to $\lambda = 100$ m and the Von Karman correlation function can be applied to fine grids in which we will model interpolation errors.

3.3. Altimetry-Predicted Bathymetry Uncertainty Model

To model bathymetry uncertainties, we adopt a stochastic approach that uses a random field and use accurate shipboard measurements (e.g., single beam and multibeam measurements) to constrain the

uncertainties. The SRTM15+V2.0 global DEM (Tozer et al., 2019), for example, contains shipboard soundings in ~11% of the grid cells. In this study, we assume that errors of the shipboard data are negligible compared to ϵ. To combine the altimetry-predicted bathymetry uncertainty with the complementary shipboard data, we model the bathymetry uncertainty as a conditional random field. In this way, regions with no shipboard data nearby will have uncertainty determined by ϵ, while regions with shipboard data nearby will have smaller uncertainties. It is noteworthy that alternative approaches based on weighting functions have been proposed to reduce uncertainty close to shipboard data (Timko et al., 2017). We think that conditional random fields better simulate the spatial extent of the sounding data influence, which will be comparable to the correlation lengths.

The modeling of conditional non-Gaussian random fields is difficult, and analytical solutions are only found for special cases. We propose a simple strategy: First, we define a conditional Gaussian random field model, whose samples can be obtained with standard procedures; second, these samples are transformed into a non-Gaussian random field by means of a translation model. The conditional Gaussian random field is defined by the covariance c_b and mean μ_b with the forms (e.g., Grigoriu, 2012; Kelker, 1970)

$$c_b(x_i, x_j) = c_{p11} - c_{p12}(c_{p22})^{-1}c_{p21}, \tag{7}$$

$$\mu_b = \mu_{p1} + c_{p12}(c_{p22})^{-1}(z - \mu_{p2}), \tag{8}$$

where z is the vector with known depths at the directly measured locations (i.e., where bathymetry is assumed to be certain), and the matrices c_{p11}, c_{p22}, c_{p12}, and c_{p21} are blocks of the unconditional covariance matrix c_p over the bathymetry domain. c_p is equal to c in Equation 6, with $H = 0.975$, $a_x = a_y = a = 4$ km and $\sigma_e = 160$ m. c_{p11} are the covariance terms between the locations with uncertain depths (i.e., grid points with errors), c_{p22} are the covariance terms between the locations with known depths (i.e., accurately measured locations), and c_{p12} are the covariance between locations with uncertain (rows) and certain (columns) depths. Finally, $c_{p12} = c_{p21}^T$. The vector μ_{p1} contains the mean of field positions which have uncertain depths, while μ_{p2} contains the mean of the positions with known values. Here, measured locations are assumed to have no errors and $\mu_{p2} = z$. The resulting $c_b(x_i, x_j)$, μ_b and uncertainty model are nonstationary (i.e., not homogeneous).

3.4. Synthetic Bathymetry Sample Generation

The samples of the conditional Gaussian random field, $G(\omega)$, are built by adopting a Karhunen-Loeve (K-L) expansion (Grigoriu, 2012; Sepúlveda et al., 2017). The K-L expansion uses an eigenvalue decomposition of the covariance matrix to model random field samples as a superposition of uncorrelated modes, each of them multiplied by a random number (i.e., one random dimension per mode). The K-L expansion presents some advantages compared to other classic methods (e.g., Fourier transform methods with random phases). For example, it is sufficiently robust to be applied to nonsquare domains and to model nonhomogeneous random fields. The expansion is expressed as

$$G(\omega) = \mu_b + \sum_{j=1}^{N} \Psi_j \sqrt{\lambda_j} Z_j(\omega), \tag{9}$$

where $G(\omega)$, μ_b, and Ψ_j are vectors representing the values in the field, the mean, and the jth covariance eigenmode, respectively. λ_j is the jth eigenvalue. $Z_j(\omega)$ is a random number sample which is uncorrelated with the random number samples of other terms of the expansion. For the particular case of a Gaussian random field, the values of $Z_i(\omega)$ are independent and follow a normal distribution with zero mean and unit variance. They can be simply obtained using a normal random number generator, such as *normrnd*(0, 1) in Matlab. N represents the number of eigenmodes included in the expansion. The accuracy of the K-L expansion can be measured by the loss of variance as a consequence of the expansion truncation (Grigoriu, 2012)

$$\epsilon_{var}(i) = \frac{\sum_{j=1}^{N} \Psi_{i,j}^2 \lambda_j - \sigma_e^2}{\sigma_e^2}. \tag{10}$$

An analysis of the K-L truncation and accuracy is given below. Finally, the conditional Gaussian random field samples are transformed to random field samples with a Laplacian marginal distribution, $B(\omega)$. We apply a translation with the form

$$B_i(w) = \begin{cases} \sqrt{\sigma_{ei}/2}Log[2\Phi(G_i(\omega))], & \text{for } G_i(\omega) < \mu_{ei}, \\ -\sqrt{\sigma_{ei}/2}Log[2(1-\Phi(G_i(\omega)))], & \text{for } G_i(\omega) \geq \mu_{ei}, \end{cases} \quad (11)$$

where μ_{ei} and σ_{ei} are the error mean and standard deviation at location i, $G_i(\omega)$ is a sample of the Gaussian random field at location i, and Φ is the Gaussian cumulative density function. The translation is a nonlinear function transforming not only the marginal distribution but also the covariance function of the final samples. While the analytical relation between the correlation coefficients of the Gaussian and the corresponding non-Gaussian random fields only exists for special cases (e.g., translating from a Gaussian to a log-normal marginal distribution in Sepúlveda et al., 2017), Grigoriu (1995) indicated that the translation produces small modifications to the correlation coefficient function when the latter is strictly positive. This is the case for Equation 6. Hence, the Gaussian random field samples of this study are built by specifying the same Von Karman covariance in Equation 6. Now, we apply the uncertainty model and the sampling generation method to produce synthetic bathymetry samples for northern Chile.

3.4.1. Sample Generation for Synthetic High Wavenumber Bathymetry

We create synthetic bathymetry samples for northern Chile by combining the predicted long wavelength component of the altimetry-predicted bathymetry with short wavelength error samples generated using our uncertainty model. The SRTM15+V2.0 DEM (Tozer et al., 2019), which has a 15 arcsec grid resolution (~500 m), provides the long wavelength component. The methodology is robust enough to be applied to any DEM combining altimetry-predicted bathymetry with complementary highly accurate measurements. The SRTM15+V2.0 DEM data are extracted for two grids, which are shown in the left panels of Figures 4a and 4b. For Grid 1, we undersample the number of grid nodes from the DEM, so we reach a resolution of 1.5 arcmin. For Grid 2, we use the original resolution of the DEM, equal to 15 arcsec. Accurate shipboard soundings are shown as black dots in the right panels of Figures 4a and 4b, which are provided in a data information grid file for the SRTM15+V2.0 DEM (known as source identifier, SID). This information is assumed to be certain. We further assume that the low coastal topography has no uncertainty, because topography data are often more accurate than bathymetry. These certain low topography data are used to constrain bathymetry uncertainty close to the coast (i.e., is considered in the construction of random field samples). Higher topography data are certain as well but do not constrain the bathymetry uncertainty. For the uncertainty model, we use $a = 4$ km, $H = 0.975$, and $\sigma_e = 160$ m, and the DEM is adopted as the mean bathymetry (i.e., left panels of Figures 4a and 4b). The computed standard deviation of the uncertainties are shown in the right panels of Figures 4a and 4b. Low values of standard deviations are reached close to the survey data. Grids 1 and 2 contain 222,742 and 48,960 nodes, respectively. Such a large number of nodes requires very large unconditional and conditional covariance matrices, which demand a large amount of computer memory for their storage. To reduce the computational demand, a reduced number of grid nodes can be selected, depending on the type of study. For instance, tsunami waves are affected by bathymetry uncertainties when the latter are comparable to the total water depth (as tsunami propagation depends on the total water depth). Consequently, we may only assign uncertainties to the grid nodes at depths shallower than a certain threshold. In our illustration case below, for example, we specify uncertainties at mean depths shallower than 3 km, where the uncertainty standard deviations (i.e., $\sigma_e = 160$ m far from data) are at least 5% of the mean water depth. Nodes in deeper zones are removed from the uncertainty model. Figures 4a and 4b show that the uncertainty standard deviation is zero for mean depths deeper than 3 km (see the −3 km isobath).

The accuracy of the generated samples depends on the truncation of the K-L expansion (i.e., Equation 10). Figure 5 shows the median relative errors of the variance for the nodes of Grids 1 and 2. Grid 1 requires more than 4,500 K-L terms to obtain median relative errors smaller than 20%. Grid 2, on the other hand, reaches the same accuracy with less than 1,000 K-L terms. For a given accuracy, more K-L terms are required for larger grids and shorter correlation lengths. For our illustration case, we use a total of 4,600 K-L terms for all grids.

Figures 6a and 6b show three realizations of the synthetic bathymetry samples that include the error from the synthetic high wavenumber content. The left panels show the certain shipboard survey soundings for depths

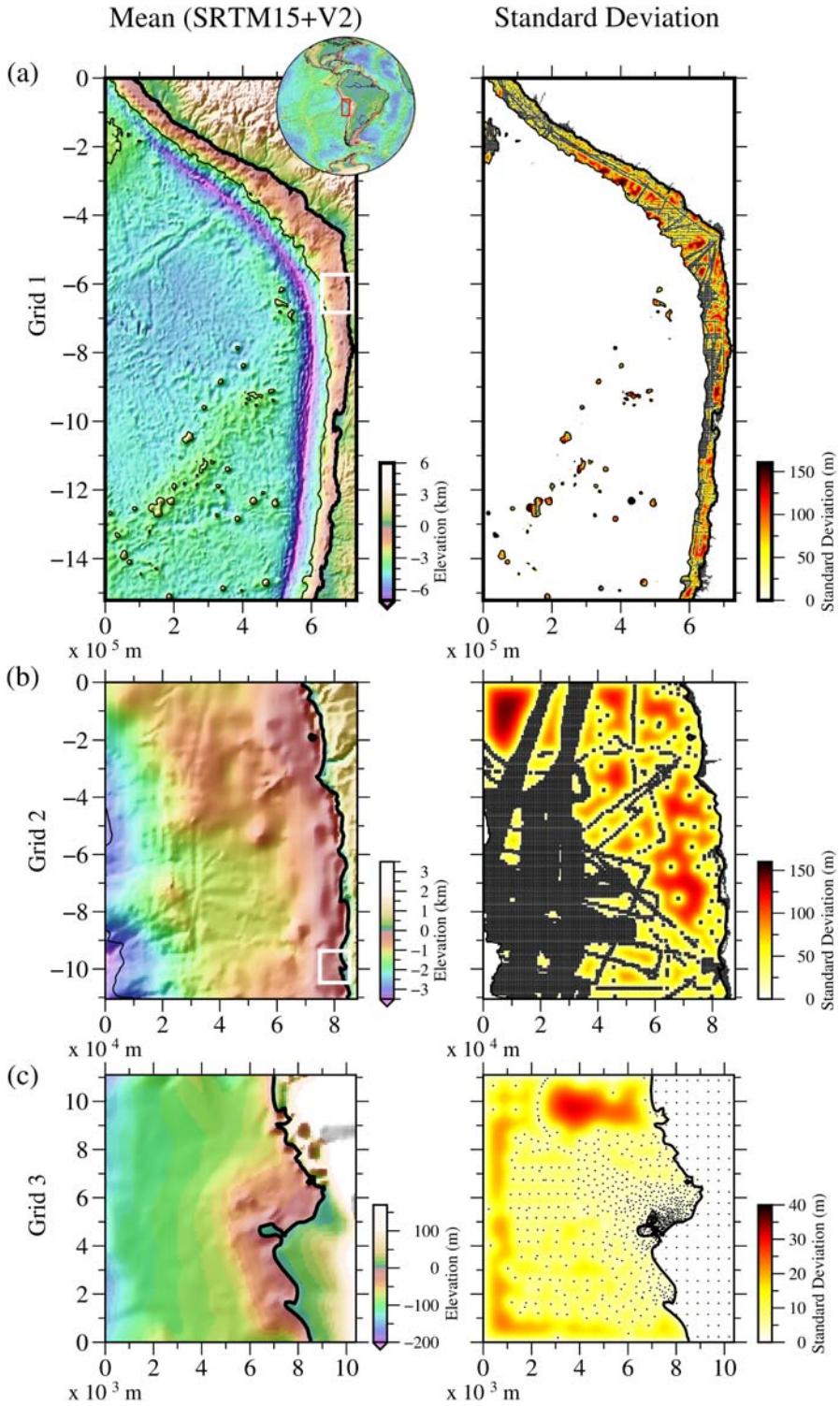

Figure 4. Mean and standard deviation of the bathymetry uncertainty model. Rows (a), (b), and (c) correspond to grids 1, 2, and 3, respectively. The mean bathymetry of Grids 1 and 2 is equal to the SRTM15+V2.0 DEM. The Grid 3 mean is based on the interpolation from shipboard sounding data within the grid. The black dots in the right panels show accurate shipboard survey data and low topography data constraining bathymetry close to the coast. The data of Grids 1 and 2 are extracted from the SRTM15+V2.0 SID file. The survey data of Grid 3, on the other hand, are obtained from soundings from a nautical chart used in this study (SHOA, 2009). The thick black contours are the coastline and the thin black contours indicate the 3 km isobath relative to mean sea level. Areas shallower than 3 km are assigned an uncertainty in the uncertainty model. White rectangles show the location of the higher resolution grids.

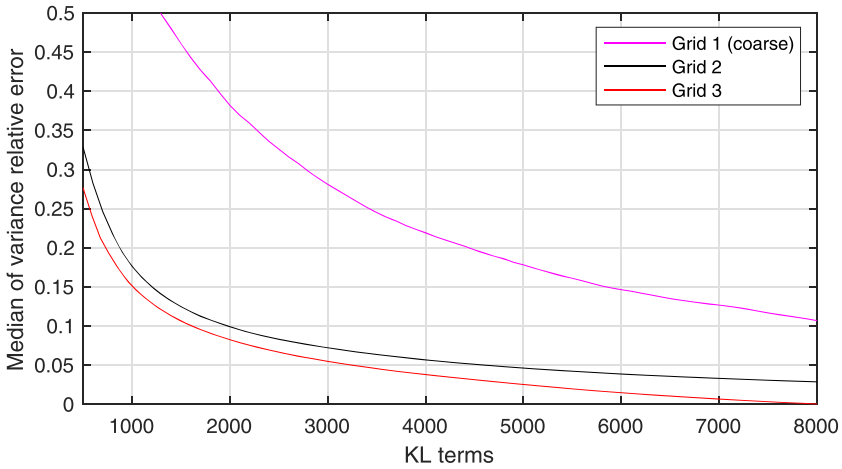

Figure 5. Median relative errors of the variances for the nodes of Grids 1, 2, and 3 as a function of the number of terms of the K-L truncation. We use 4,600 K-L terms for all the grids to achieve median relative errors of 20%, 5%, and 3% for Grids 1, 2, and 3, respectively.

shallower than 3 km and low topography data (constraining bathymetry uncertainties close to the coast) as black dots. The corresponding error samples (i.e., synthetic high wavenumber content samples) are also shown in Figure S2. The contribution of the synthetic high wavenumber content is evident after comparing the mean bathymetry of Figure 4 and the samples of Figure 6. Figure 7 shows a comparison between the target probability properties (i.e., a Von Karman covariance function with $H = 0.975$ and $a = 4$ km, a Laplacian distribution, and $\sigma_e = 160$ m at unconditional areas) and the statistics of 20,000 samples. We observe that statistics are very close to the target probability properties. Some small deviations are seen because of K-L truncation and translation errors. The largest, but still small, errors are found for Grid 1, which has the largest K-L truncation errors.

Different grids are commonly nested in numerical models in order to vary the resolution. The mean bathymetry of different grids are equivalent at the same locations (e.g., at the edges of the finer grids) because they are equal to the DEM. Hence, the mean bathymetry is expected to be continuous where coarser and finer grids connect. However, the bathymetry samples generated with additional uncertainty are independent among the different grids and, therefore, may present significant discontinuities where grids connect. To remove spurious discontinuities, the finer grid is modified at the edges so that its bathymetry is equal to the corresponding bathymetry sample of the coarser grid. We modify the finer grids in a buffer zone of 3 km from each edge, which is comparable to the uncertainty correlation length. To include uncertainty once within the buffer zone, we remove the uncertainty of the finer grid model (i.e., we only consider the uncertainty of the coarser grids at the edges of the finer grid).

3.4.2. Sample Generation of Uncertain Bathymetry in High-Resolution Grids

We now employ the uncertainty model and sampling method to quantify the uncertainties when high-resolution shipboard soundings are interpolated. Some form of interpolation is commonly employed to generate uniform and fine bathymetry grids. This is often the case for tsunami propagation models in which bathymetry sampling finer than 100 m is required in coastal areas for accurate simulations. As we noted above, the spectral amplitude of ϵ is expected to be equal to that of the high wavenumber content of the true bathymetry. When the distance between the interpolated shipboard soundings is shorter than ~10 km, we can use the same uncertainty model to add high wavenumber variability, which is not resolved by the interpolation.

The left panel of Figure 4c shows an interpolated bathymetry grid generated by sounding data in the port of Iquique, Chile. We use a cubic interpolating function, which has been observed to generate small spurious signals at high wavenumbers (i.e., at small length scales). The soundings used in the interpolation are obtained from the nautical chart of the area (SHOA, 2009) and are assumed to be highly accurate and

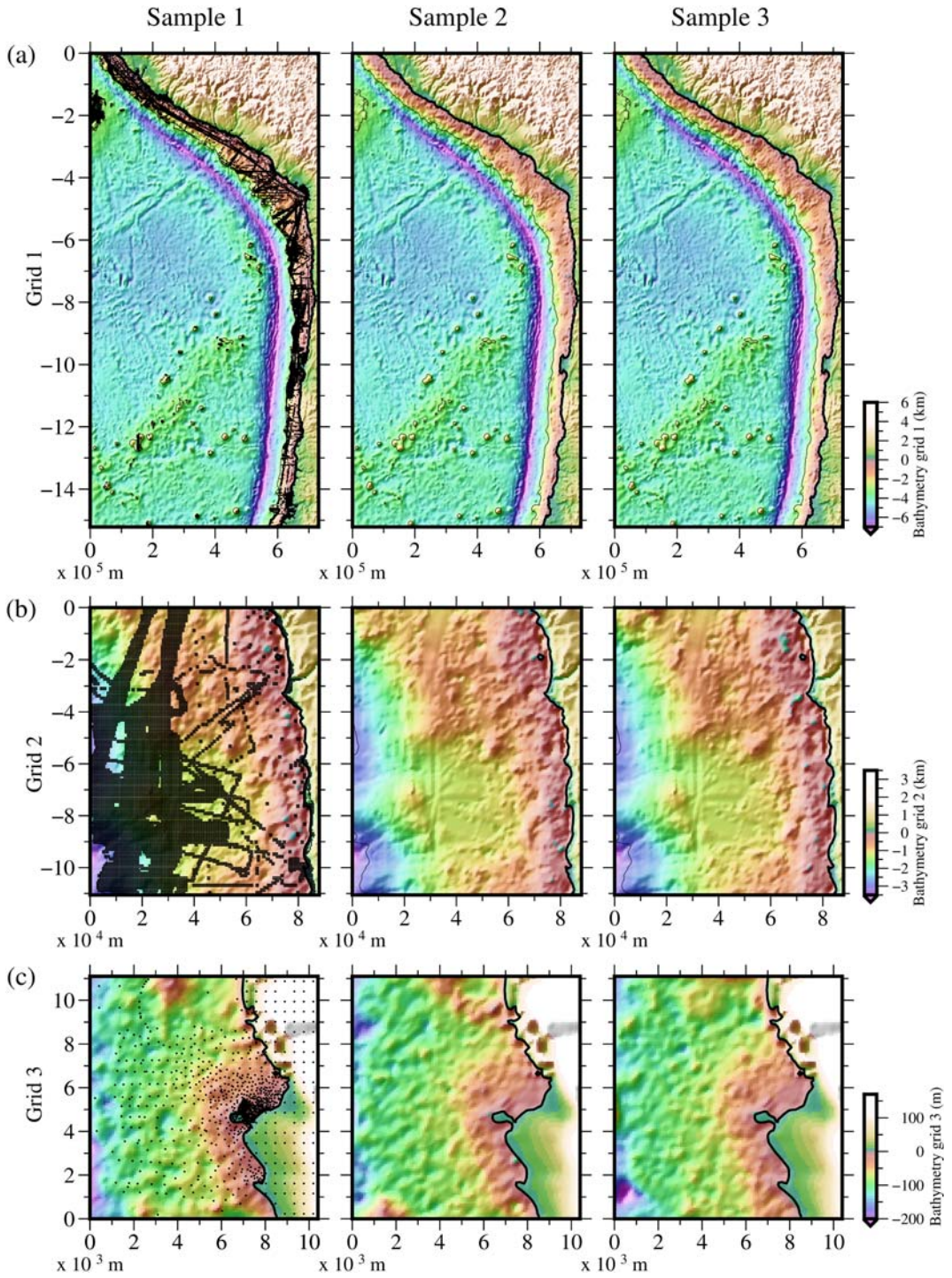

Figure 6. Three realizations of synthetic bathymetry samples for Grids 1 (a), 2 (b), and 3 (c). For spatial continuity, the two finer grids have a buffer region of 3 km at the borders. The continuous black line is the coastline, and the thin black line is the isobath at −3 km. Seafloor depths shallower than 3 km are assigned a value of uncertainty. Black dots in the left panels show data that are considered to be certain and which are not assigned a value of uncertainty for the random sample generation (i.e., shipboard survey soundings and low topography containing bathymetry close to the coast).

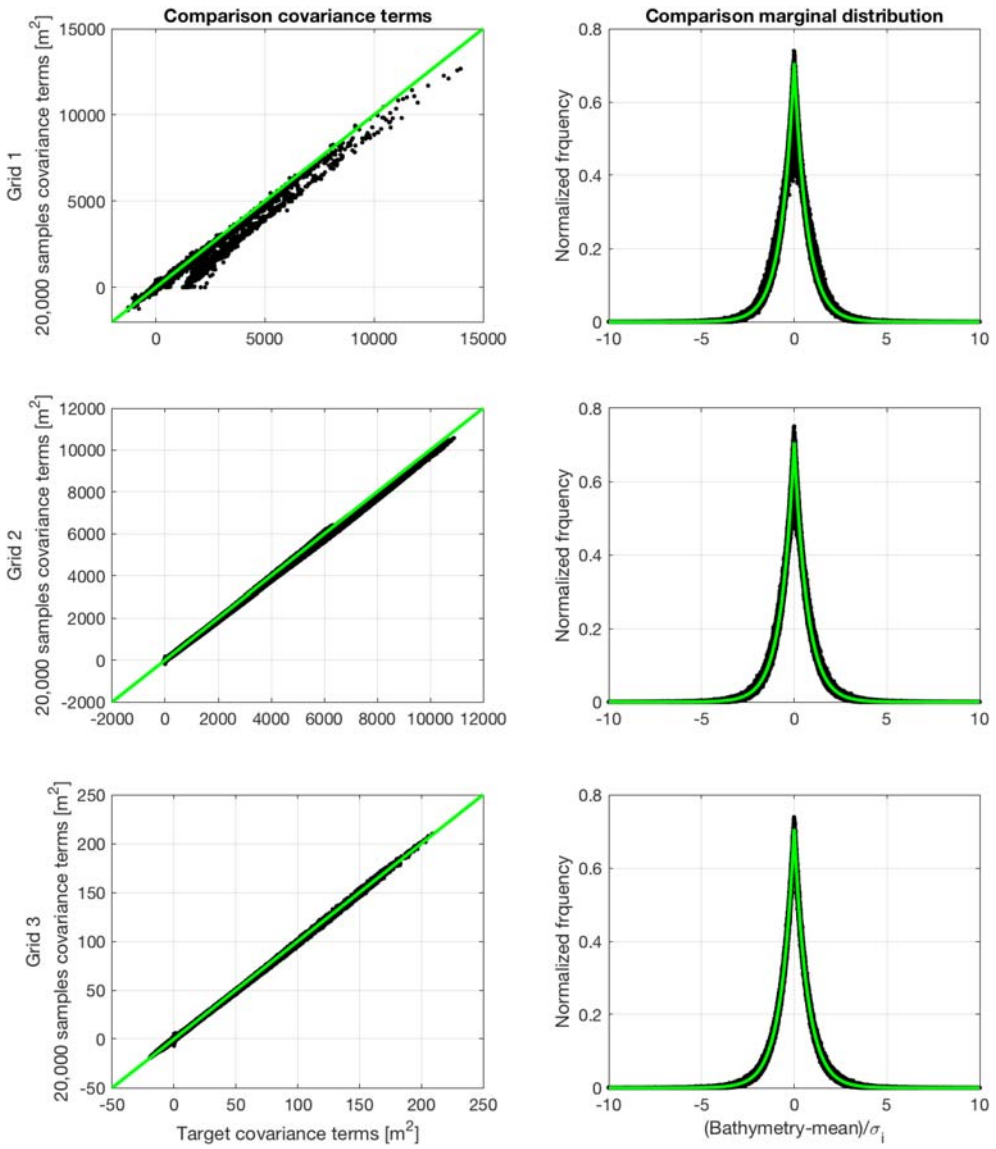

Figure 7. Comparison of 20,000 sample statistics and target probability properties for the uncertainty models of the three grids. Left panels show a comparison of the covariance terms. Green line is the 1:1 relation. The right panels compare the histograms of the synthetic high wavenumber content for each grid node and the target Laplacian distribution (depicted in green). The histograms and distributions for each grid node are normalized by the corresponding standard deviation.

certain. The resolution of the grid is finer than the average spatial density of the soundings, and, therefore, the interpolated grid is affected by uncertainty.

To model the uncertainty of the interpolated grid, we first generate an unconditional random vector, which includes the grid nodes and the highly accurate sounding locations (which are not exactly located at the grid nodes). Then, a conditional random field is built, conditional to the soundings. The standard deviation of the uncertainty model is shown in the right panel of Figure 4c. Grid nodes close to the soundings have small values, as expected. We also show the accuracy of the uncertainty model as a function of the K-L truncation in Figure 5 and a validation of the statistics of bathymetry samples in Figure 7, which are described in detail above for Grids 1 and 2. Figure 6c shows bathymetry samples, and Figure S2 shows error samples. For Grid 3, we specify values equal to that of the coarser Grid 2 samples in a buffer region within 3 km of the borders.

4. Tsunami Hazard Assessment in Chile With Consideration of Uncertain Bathymetry

In this section, we aim to quantify the uncertainties of a tsunami hazard assessment due to uncertainties in the altimetry-predicted bathymetry for an example case in northern Chile. We assess the tsunami triggered by the 2014 M_W 8 Iquique earthquake and use the initial surface elevation condition of the tsunami estimated by An et al. (2014), which is shown in Figure S3. To predict the tsunami initial condition, An et al. (2014) used DART buoy records and a tsunami source inversion solving for the earthquake slip distribution. A validation of the inversion was also conducted by performing a forward tsunami simulation and comparing simulated coastal responses with tide gauge records. The comparison of An et al. (2014) (Figure 6 of that paper) showed that simulations fit the leading wave amplitudes fairly well at most of the stations. However, significant misfits on the arrival times and trailing wave amplitudes were observed at some stations. While sources of such errors are still unknown, bathymetry uncertainties were hypothesized as one possible source. Hence, in this application case, we aim to understand the impact of bathymetry uncertainties on the tsunami propagation.

For the propagation of uncertainty from the bathymetry to the tsunami response, we adopt a Monte Carlo approach and use the COMCOT tsunami model to solve the nonlinear shallow water equations with an explicit leapfrog finite difference scheme (Wang, 2009). The numerical grids, where the tsunami responses are calculated, are the same grids as shown in Figure 4. Different grid resolutions are required to satisfy criteria for the typical wavelengths of tsunami waves, which change during the shoaling process, so three nested grids are used. We simulate bottom friction using the Manning formula with coefficient 0.03 (Bricker et al., 2015) and simulate the tsunami runup using a moving boundary scheme (Wang, 2009). We conduct a sensitivity analysis to determine the number of samples required to get accurate estimates of the tsunami response statistics, and we find that 1,000 samples are necessary for the convergence of statistics (i.e., convergence of 95% percentiles). The statistics obtained with 1,000 samples are as accurate as those obtained with 3,000 samples (see Figure 9b). This reasonable number of samples has important implications because it shows that regardless of the high number of random dimensions necessary to accurately describe bathymetry uncertainties (e.g., at least 4,600 for Grid 1), the tsunami response seems to be affected by a smaller number of dimensions (otherwise, we would require a much greater number of samples). The number of required samples could possibly be further reduced by adopting better uncertainty propagation methods such as SROM (Sepúlveda et al., 2017) or by implementing a surrogate model (Liu & Guillas, 2017). The number of required bathymetry samples may change for other regional tsunami hazard assessments.

4.1. Uncertainty Statistics Within the Tsunami Model Domain

We compute the maximum tsunami surface elevation for each simulation, which is defined as the maximum surface elevation reached during 120 min of tsunami propagation. Then, we compute the second moment properties. The mean maximum tsunami elevations, shown in Figure 8a, have values larger than 1 m in the tsunami generation zone and at the coast. In some coastal areas, we observe a significant amplification of the tsunami wave likely due to shoaling and coastal resonances. For example, in Iquique port, we observe large values within the port, exceeding 2 m (i.e., right panel in Figure 8a). A comprehensive measure of the uncertainty of the maximum tsunami elevation is the variance, which is shown in Figure 8b. To highlight the differences of the tsunami response uncertainty, the variance is plotted in a logarithmic scale. We observe that the uncertainty in the maximum tsunami elevation is near zero in the generation zone. In this region, the maximum elevation occurs at an early time (at or near the initial time). At that time, the tsunami wave has propagated a short distance or has not propagated at all, and the bathymetry uncertainty does not affect the long waves. As tsunami waves propagate longer distances, uncertainty effects increase. The impact of bathymetry uncertainties depend on the mean bathymetry. In deeper water regions (i.e., west of the source region), the highest tsunami waves propagate through areas where uncertainties are much smaller than mean water depths. As a consequence, the impact of the uncertainty on tsunami propagation is small there. However, we observe an increase of uncertainty in areas of shallow depths and farther away from the tsunami source, in particular at the southwestern corner of Grid 1 (Figure 4a). Close to the continental coast, we observe a strong increase of the maximum tsunami elevation uncertainty.

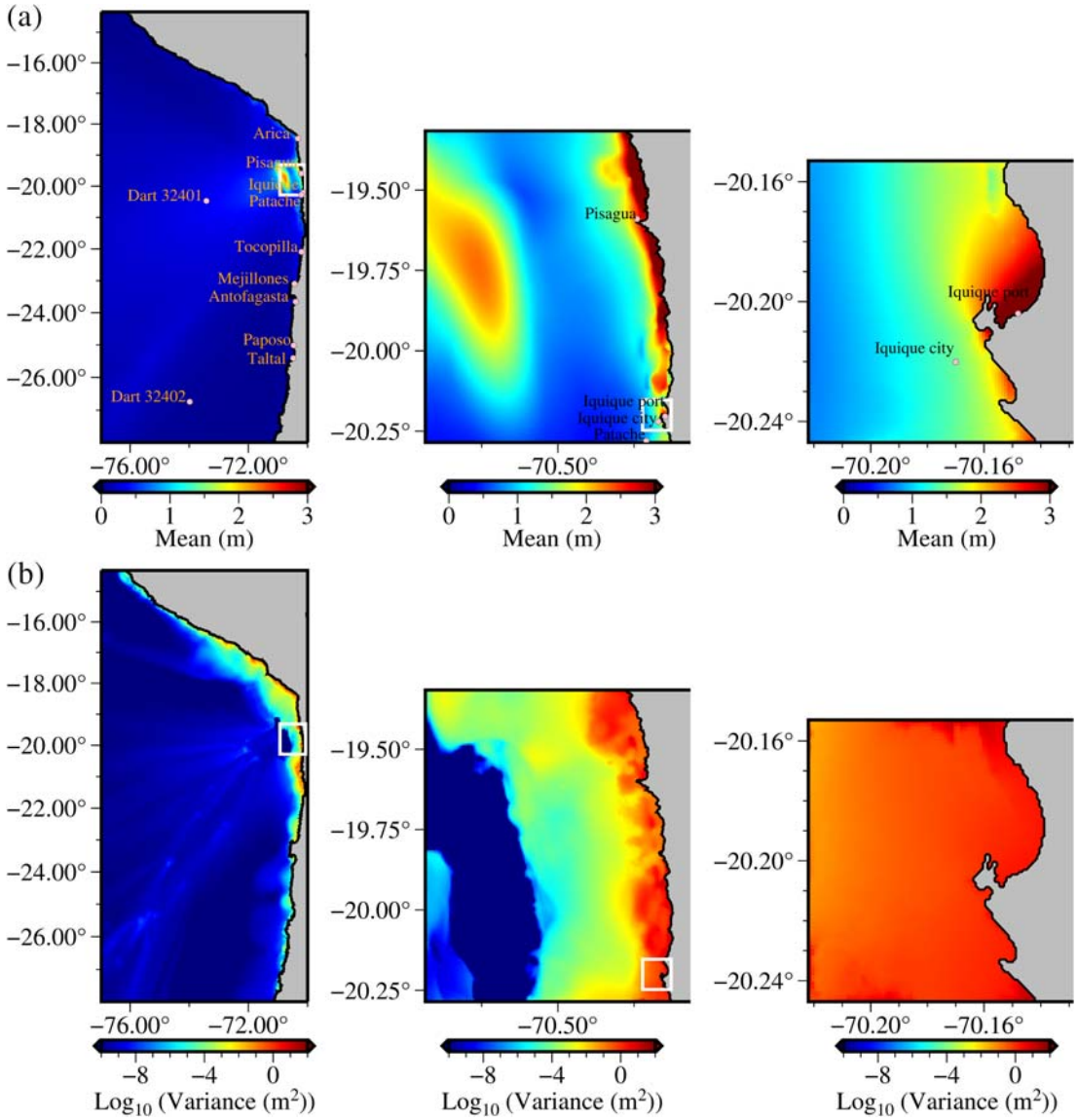

Figure 8. Mean (a) and variance (b) of the maximum tsunami elevation affected by bathymetry uncertainties. The variance is presented with a logarithmic scale.

4.2. Uncertainty in Tsunami Elevation Time Histories

To gain more insight into the response of tsunami waves and their uncertainty, we analyze tsunami time histories at 12 gauges in the middle and near field, which are depicted by orange dots in Figure 8a. The gauges at Iquique port and Iquique City are located within Grid 3 and show the impact of bathymetry uncertainty at locations where bathymetry data are spatially dense. Both locations also illustrate the uncertainty variations in coastal areas. For instance, Iquique port is located inside a bay, apparently affected by tsunami wave resonance, while Iquique city gauge is outside the bay. DART32401 and DART32402 show the effect of bathymetry uncertainties at offshore buoys, which are commonly used for tsunami early warning and and have also been used for tsunami source inversions, because leading waves arriving there are usually not affected by nonlinearity. The eight additional coastal gauges at Arica, Pisagua, Patache, Tocopilla, Mejillones, Antofagasta, Paposo, and Taltal are included to show the impact at coastal locations where only coarse bathymetry data are available and where the simulation equations are solved on coarse numerical grids. Coarse grids are commonly used for early-warning tsunami models, which require fast computation (Titov & Gonzalez, 1997). All of the gauges are located in water, including the coastal ones near the shoreline. However, a few bathymetry samples are generated with one or two gauges located on land (i.e., above the water

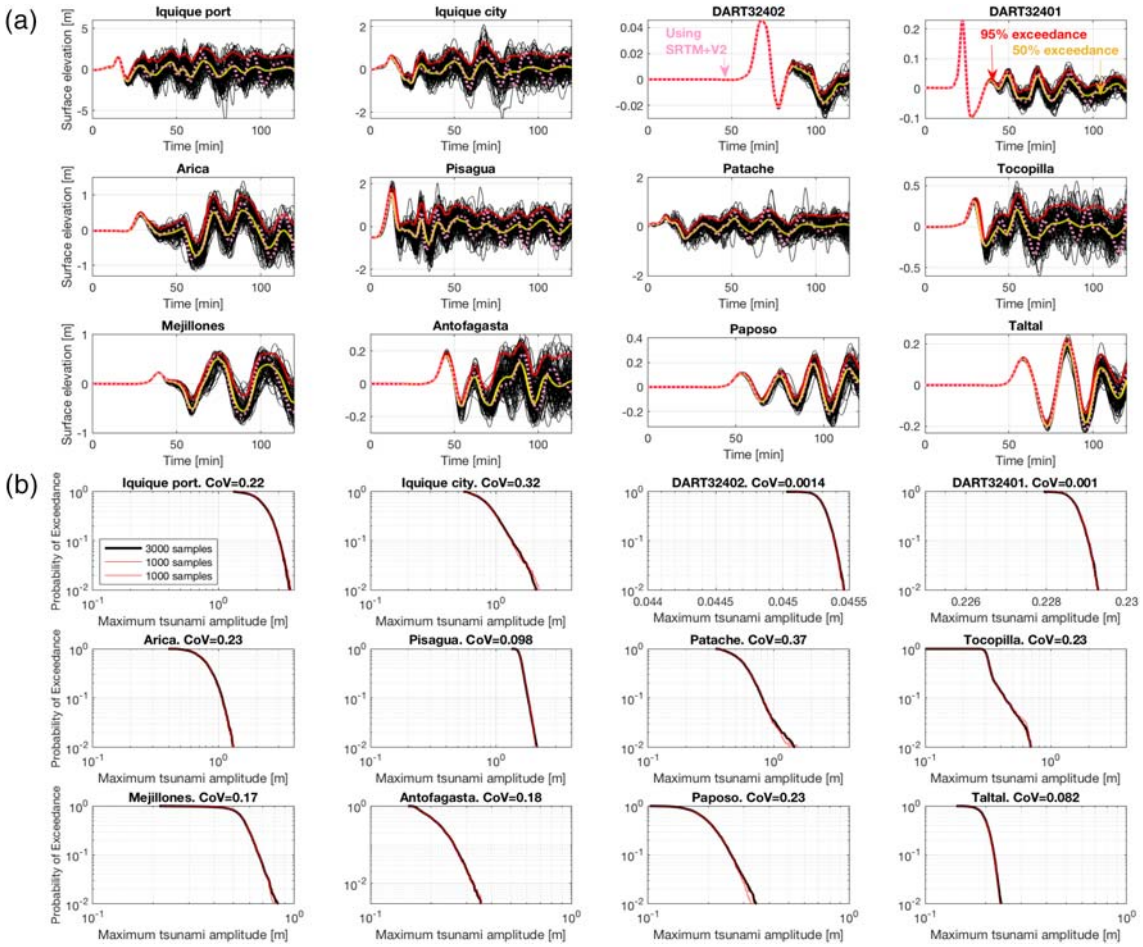

Figure 9. (a) Time histories of the tsunami water elevation at 12 tide gauge and buoy locations. Yellow and red curves represent the 50% and 95% exceedance probabilities, respectively. The pink dashed curves represent a tsunami simulation with no bathymetry error. (b) Exceedance curves for the maximum tsunami water elevation at the 12 locations. The black lines correspond to Monte Carlo simulations with 3,000 samples. The two red lines correspond to different Monte Carlo simulations with 1,000 samples.

surface elevation) because the random bathymetry error is larger than the water depth. Those samples are removed from the analysis.

Figure 9a shows time histories of the tsunami elevation at the 12 gauges shown in the map in Figure 8a. For each location, we show the 50% and 95% exceedance probabilities for the water surface elevation at every time, as well as a tsunami simulation without any bathymetric error added. In general, we observe that leading waves are less affected by the bathymetry uncertainty, compared to the trailing waves. We also observe that arrival times are practically unaffected by bathymetry uncertainties. While tsunami wave periods present more variability among the tsunami samples, the differences are small for the first waves (i.e., leading and second waves). The uncertainty of trailing waves is diverse at the 12 gauges, and it seems to be independent of the surrounding water depths. Figure 9b also presents exceedance curves of the maximum tsunami elevation and the corresponding coefficient of variation (COV) for each of the gauges. The COV is defined as the maximum tsunami elevation standard deviation divided by the mean and describes the intensity of the maximum tsunami elevation uncertainty as compared to the mean value. The largest COV values are located at the Arica, Iquique city, Paposo, Patache, and Tocopilla coastal gauges, associated with the maximum elevations occurring in trailing waves. The smallest COV values correspond to the offshore buoys DART32401 and DART32402, in which the maximum tsunami elevations correspond to a leading wave propagating through significant water depths.

The results of Figure 9 show that uncertainty is relevant only when two conditions are present. First, bathymetry uncertainties have to be comparable to water depths, so celerity of long waves is significantly

modified and propagation can be altered. Leading waves propagating from the source to the west, for example, have smaller uncertainty than leading waves arriving at coastal gauges. Second, tsunami wavelengths have to be comparable to the characteristic length scale of the bathymetry uncertainty, which in this study is represented by the uncertainty correlation length. Trailing waves of the coastal gauges, for instance, occur after leading waves approach the coast and shorter waves are generated as a consequence of the irregular topo-bathymetry. Those shorter waves are then more affected by the high wavenumber content of the bathymetry, which is uncertain. Thus, our results show that bathymetry uncertainties are not the main cause of the significant misfits observed in the comparison between the tsunami records and model results of An et al. (2014).

While trailing waves are more affected by bathymetry uncertainties, compared to the leading wave, the accuracy of their estimation may be challenged by physical processes which are ignored by the shallow water wave theory. For instance, as waves become shorter wavelength and higher amplitude, frequency dispersion may become relevant. Furthermore, wave breaking at the coast is not considered. A more accurate quantification of trailing wave statistics may require more sophisticated tsunami models that include frequency dispersion and wave breaking. In the tsunami model above, we have also specified a constant Manning coefficient to model bottom friction. Bottom friction, though, depends on the high wavenumber content of the bathymetry. Therefore, the inclusion of bathymetry high wavenumber content (and the bathymetry uncertainty model) may also need to be considered in the bottom friction model. Our bathymetry uncertainty model specifies low topography as certain because it is often much more accurate than the altimetry-predicted bathymetry. However, coastal topography data may suffer by errors in the order of tens of centimeters to meters. These errors may be relevant when tsunami inundation depths are comparable. As a consequence, the tsunami runup and inundation processes for the leading wave may also have larger uncertainties than those obtained at the analyzed coastal gauges.

5. Estimating Statistics of Altimetry-Predicted Bathymetry Errors (ϵ) in the Oceans

In section 3, we demonstrated that the statistics of ϵ for the seafloor off the Chilean coast can be modeled reasonably well by using the Von Karman and Laplacian functions for the correlation and marginal distribution, respectively. This poses the question about whether the statistical model (i.e., a Laplacian marginal distribution and a Von Karman correlation function with parameters a, H, and σ_e) can be generalized to use for any region of the oceans. This question is especially pertinent for regions where multibeam data are not available. We conduct the statistical analysis of section 3 for the remaining 13 regions shown in Figures 1 and 2. Two samples exhibit small artifacts, likely derived from the multibeam surveys (i.e., small artificial "banding" in Regions #7 and #14 in Figure 2). We decide to include these samples because the artifacts are small and band-limited and so will have little impact on our analysis.

Figure 10a shows the power spectral density of ϵ. Figure 10b shows the variance-normalized power spectral density collapsed to one dimension in k. For completeness, we include the power spectral density and histograms of the multibeam data in Figure S4. The plots of the Chilean regions are presented again for the sake of comparison. Anisotropy, which is revealed by the shape of the spectra in Figure 10a and the dispersion of the black dots in Figure 10b, is stronger in some regions than others (e.g., Region 7), but it is not severe. Indeed, the width of the most dispersed dot clouds in Figure 10b is ~1.5 units on a logarithmic scale, and the power spectral amplitude ranges between 2 and 8 units. In general, the isotropic assumption is reasonable for all the 15 regions. All the samples exhibit a similar power spectral density with a constant power law decay at high wavenumbers, although that constant varies for each region.

Long- and short-scale variations of the bathymetry may be sculpted by different processes. Tectonics also plays a primary role in determining the spectral properties of the bathymetry of a given region. These types of differences can be identified in the sample regions we have selected. For example, Regions #9 and #13 show sea mounts surrounded by smooth flat sea floor. These different long- and short-scale features are also evident in the spectra of h (Figure S4) and ϵ (Figure 10b) and produce deviations from the ideal fractal behavior. For instance, Figure 10b shows that the empirical spectra of Regions #9 and #13 have greater spectral amplitude in wavenumbers of 10^{-4} m^{-1} (i.e., the seamounts) and a faster amplitude decay for wavenumbers between 10^{-4} and $10^{-3.5}$ m^{-1}, compared to the best fit Von Karman model assuming a fractal behavior at high

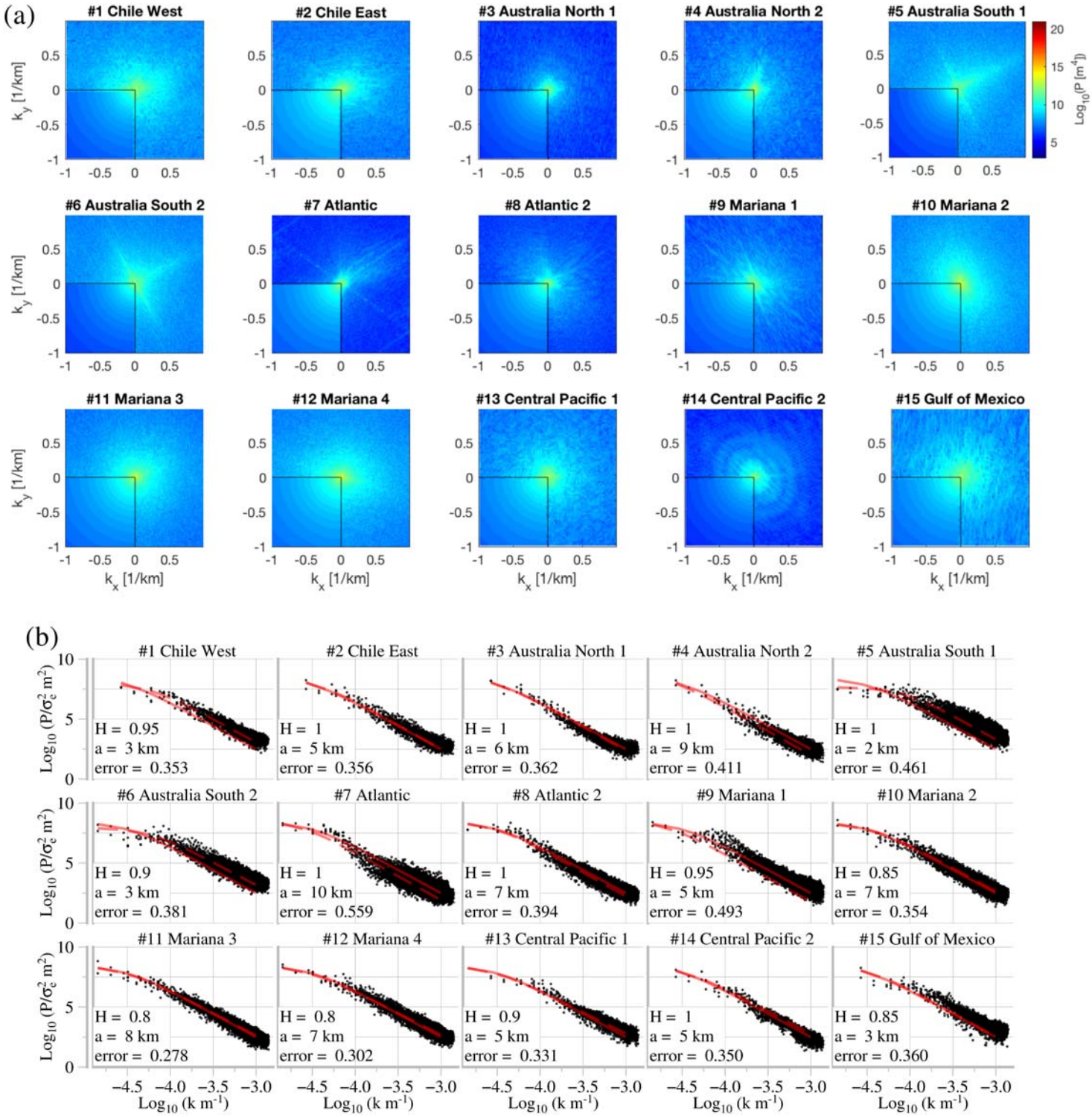

Figure 10. (a) Power spectral densities (i.e., Fourier transform of $c(\xi)$) of ϵ for the 15 regions. The lower-left corner shows the modeled power spectral density for a Von Karman function with $a_g = 6$ km, $H_g = 0.95$, and a variance predicted with Figure 11a. (b) Variance-normalized power spectral density of ϵ as a function of k. The dashed red curves correspond to the best fit Von-Karman curve for each region. Values of correlation length, a, and Hurst number, H, are given in each panel. We also report the rms error on a logarithmic scale. The Von Karman curve with the best fit to all spectra (solid red curves) has $a_g = 6$ km and $H_g = 0.95$.

wavenumbers. These deviations from the fractal behavior due to local features, however, are not severe, and the spectra smoothly decrease in amplitude with wavenumber. For example, Region #9 has deviations of ~1 unit on a logarithmic scale with the power at low wavenumbers greater than 7. To first order, all of the samples can be satisfactorily modeled with a Von Karman correlation function with some additional uncertainty due to the deviations from self-similarity. In section 5.1, we further demonstrate that such deviations do not impact the uncertainty quantification in the tsunami hazard assessment. As in Figure 3f, Figure 10b shows red dashed curves representing the Von Karman function with the best least squares fit to the observed ϵ. The values of a and H and the fitting errors are shown for each spectrum. We also present a globally fitted set of Von Karman parameters equal to $a_g = 6$ km and $H_g = 0.95$, corresponding to a power law decay of -3.90 at high wavenumbers. The globally fitted curve is shown as a red solid line in Figure 10b. The values of a_g and H_g have some moderate but evident differences with respect to the local fitted parameters. The impacts of such differences are evaluated in the next section, where the tsunami uncertainty for a specific case is quantified.

Figure 11a shows the empirical values of σ_e for the 15 regions on a logarithmic scale. Unlike a and H, the range of σ_e is very large for the 15 regions. Thus, it seems inappropriate to specify a globally fitted value, and we rather need to estimate it from information available for each region. It would be useful to pose the hypothesis that σ_e^2 can be estimated from information that we are able to recover from the altimetry data. We examine whether the variance of the detrended altimetry-predicted bathymetry (i.e., the area under the red spectra in Figure S5a), defined here as σ_m^2, can be used to predict σ_e^2 using an empirical linear regression. Linear trends are removed from the bathymetry in order to remove the effects of longer wavelengths which are not accurately captured with the finite area multibeam bathymetry. If ϵ is isotropic and the bathymetry has a known power spectral density, then σ_e, which is also the standard deviation of the bathymetry high wavenumber content, and σ_m should follow the analytic expressions

$$\sigma_m^2 = \int_{k_{min}}^{\infty} W_L(k, \bar{h}) P_T(k) 2\pi k \, dk, \tag{12}$$

$$\sigma_e^2 = \int_{k_{min}}^{\infty} (1 - W_L(k, \bar{h})) P_T(k) 2\pi k \, dk, \tag{13}$$

where the power spectral density of the detrended true bathymetry, P_T, is isotropic. The minimum wavenumber, k_{min}, is determined by the dimension of the bathymetry sample. Because $W_L(k, \bar{h})$ of Equation 3 and P_T are known, σ_e and σ_m in Equations 12 and 13, respectively, are expected to be related. We use the data from the 15 bathymetry samples to test such a relation between the variances. Figure 11a shows a scatter plot comparing σ_e and σ_m. We obtain the variances for a 75 km × 75 km size area in each of the 15 regions. For the samples with size 140 km × 140 km, we use a subsample located in the bottom-left corner that is $[0, 75\,\text{km}] \times [0, 75\,\text{km}]$. This produces a systematic linear relation, on a logarithmic scale, between σ_e and σ_m, empirically demonstrating that σ_e can be estimated from σ_m, at least in these 15 regions. By performing a linear regression, we find the best fit line to be $\sigma_e = 10^b \sigma_m^a$ with $a = 0.555$ and $b = 0.840$. Figure 11a shows the best fit line in blue. We also present the 90% and 75% confidence bounds in red and green, respectively. The blue and red lines are separated by a vertical distance of ~0.17 units. This corresponds to relative differences of 47% and −32% for the values of σ_e. Including greater areas (i.e., greater than 75 km × 75 km) and smaller k_{min} may yield modified relations, as σ_m will include lower wavenumbers. The bottom left corner of the spectra of Figure 10a shows the proposed model using the Von Karman covariance function with $a_g = 6$ km, $H_g = 0.95$, and σ_e obtained from the scaling law of Figure 11a. Most of the samples are reasonably well represented by the global power spectral density model. A few samples, though, significantly deviate from the model. The marginal distribution model for the 15 bathymetry samples is also presented. Figure 11b shows the histograms of ϵ. Many samples exhibit a distribution closer to a Laplacian distribution. Some histograms, however, significantly deviate from the Laplacian distribution, with significant skewness and nonzero mean. The deviations of these regions from the general approximate model are further described in the discussion section.

5.1. Tsunami Uncertainty Quantification Using Global Average Statistics

We use the global average Von Karman correlation and Laplacian distribution functions to repeat the uncertainty propagation for the tsunami hazard assessment in Chile. Figure 12a shows the tsunami response samples using a_g, H_g, and σ_e obtained from the scaling law of Figure 11a, equal to 141 m (for $\sigma_m = 230$ m).

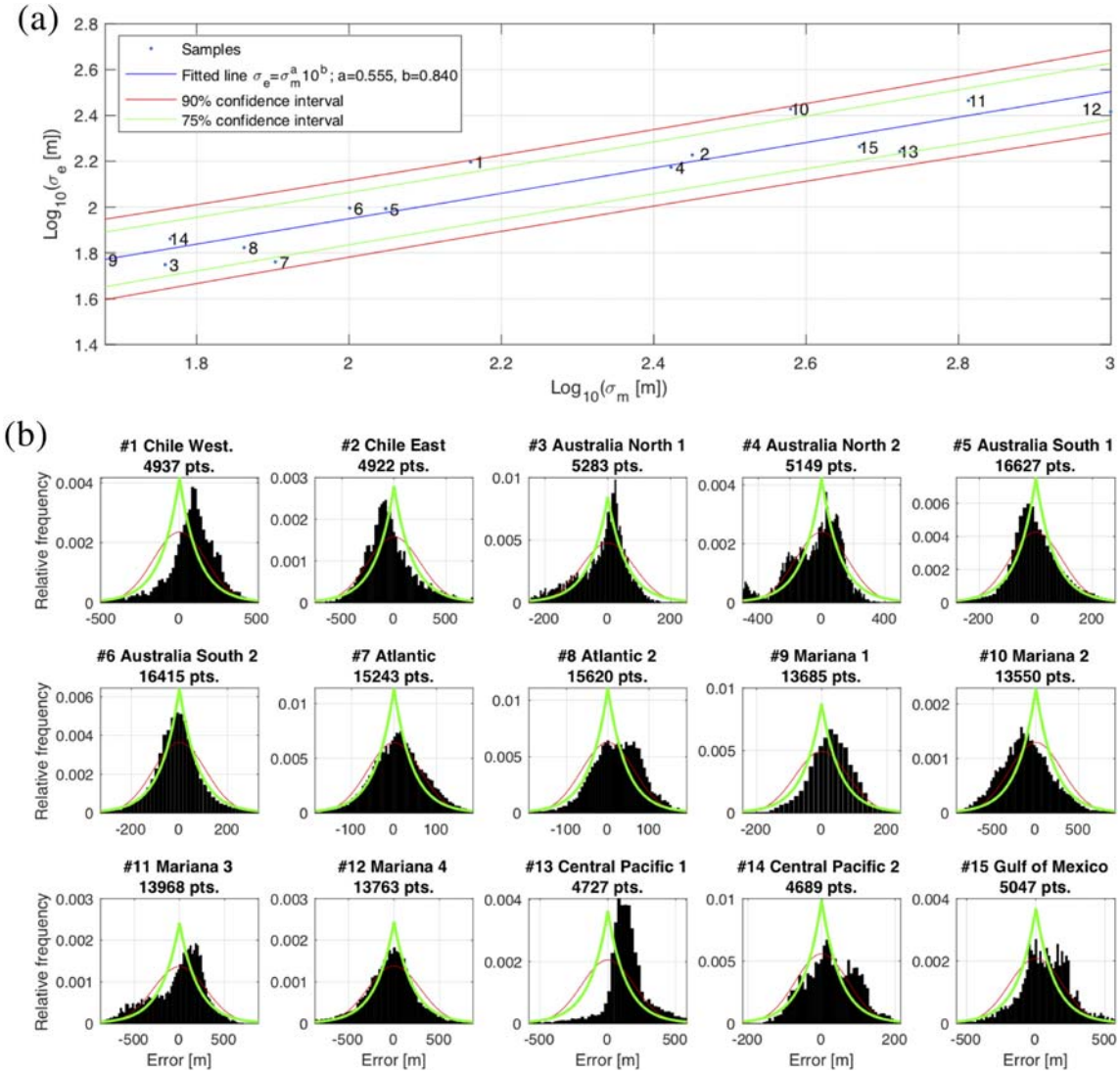

Figure 11. (a) Standard deviation of ϵ, σ_e, as a function of the standard deviation of the detrended altimetry-predicted bathymetry, σ_m. Blue numbered dots correspond to the 15 regions analyzed in this study. The blue line corresponds to the best fit, which is given by $\sigma_e = \sigma_m^{0.555} \times 10^{0.840}$. The red and green lines correspond to the 90% and 75% confidence intervals. (b) Histograms of ϵ (black bars), modeled Laplacian distribution (green line), and modeled Gaussian distribution (red line) using the same sample variance. The number of points in each histogram (i.e., at the DEM nodes) is shown in the individual panels.

The 50% and 95% exceedance curves are also presented. Figure 12b presents the new exceedance curves for the maximum tsunami elevation as red lines. As a reference, we also plot the exceedance curve of Figure 9b as black lines. The exceedance curves using $a = 4$ km, $H = 0.975$, and $\sigma_e = 160$ m are very similar to the curves using the globally fitted parameters a_g, H_g, and $\sigma_e = 141$ m. To further evaluate the stability of our tsunami uncertainty quantification results, we conduct three additional experiments in which we modify the bathymetry uncertainty properties according to the power spectral density variations seen in the 15 regions. First, we modify the correlation length from 6 to 2 km. The latter corresponds to the minimum correlation length fitted from the 15 regions (i.e., dashed red spectra of Region #5 in Figure 10b). The second experiment changes the Hurst number from 0.95 to 0.8, which corresponds to the minimum fitted value (i.e., dashed red spectra of Regions #11 and #12 in Figure 10b). The third experiment corresponds to a change of $\sigma_e = 184$ m, which corresponds to the 75% upper confidence limit (i.e., upper red line in Figure 11b). We adopt the minimum correlation length, lowest Hurst number, and larger σ_e for our sensitivity experiments because they are expected to be associated with more energy at high wavenumber, as compared to the global average parameter model. As a consequence, we expect that the corresponding tsunami responses are more uncertain in the sensitivity experiments. The green, cyan, and orange curves in Figure 12b represent exceedance

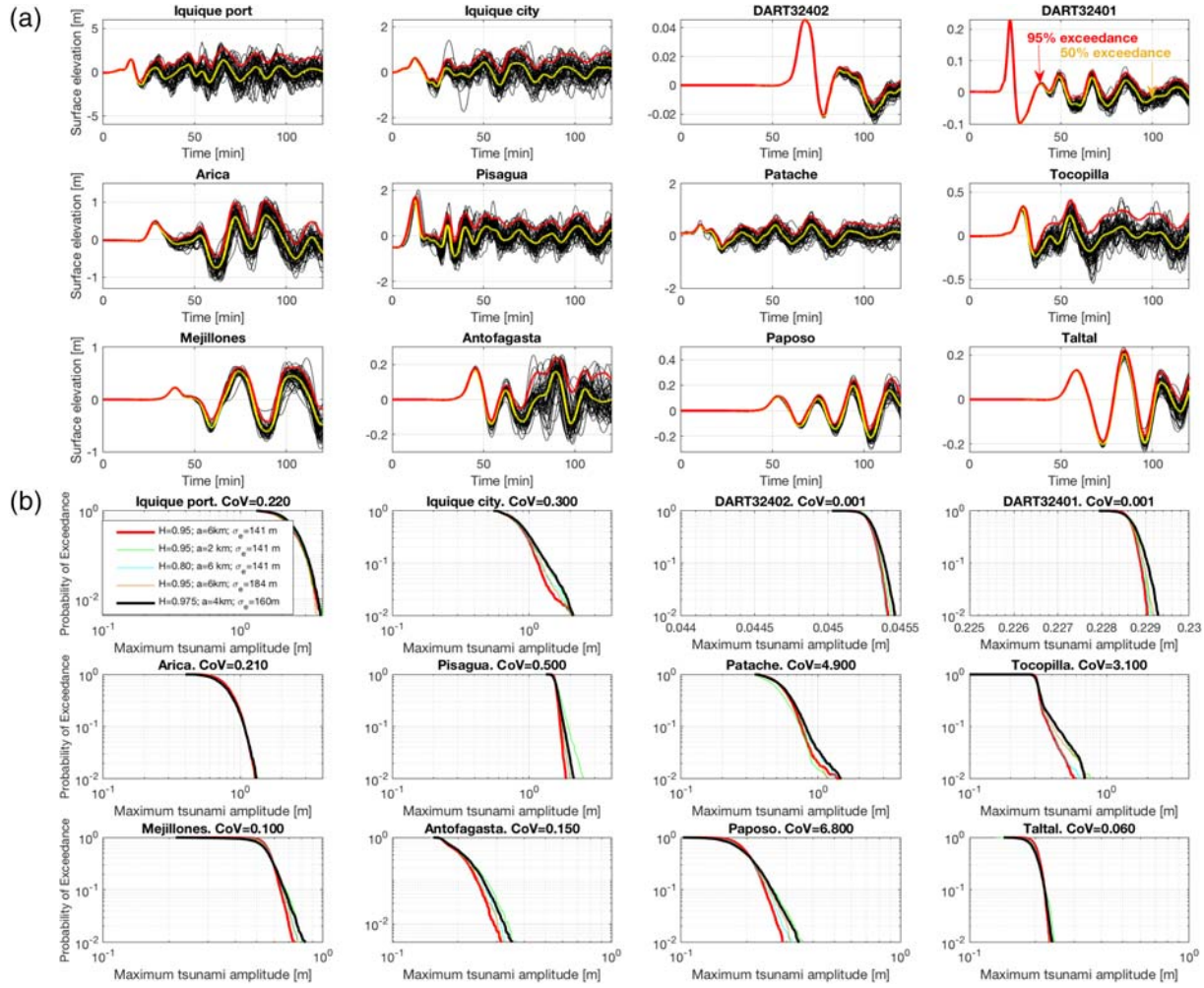

Figure 12. (a) Time histories of the tsunami water elevation at 12 tide gauge and buoy locations using bathymetry samples calibrated with globally fitted statistical properties. Yellow and red curves show the 50% and 95% exceedance probabilities, respectively. (b) Corresponding exceedance curves of the maximum tsunami water elevation at the 12 locations as red thick curves. For reference, the black curves correspond to the exceedance curves of Figure 9b. Green, cyan, and orange curves correspond to Monte Carlo simulations with a change of correlation lengths to $a = 2$ km, a change of the Hurst number to $H = 0.8$, and a change of the standard deviation to $\sigma_e = 184$ m, respectively.

curves for bathymetry with smaller correlation lengths, lower Hurst number, and larger σ_e, respectively. As observed in the 12 gauges, the uncertainty is only slightly larger than that of the preferred global and local models (i.e., red and black curves, respectively). Conclusively, tsunami response uncertainties at the selected gauges are not severely affected by the variation of the statistical properties of ϵ in the different regions.

5.2. Discussion of the Global Average Statistics of ϵ

In many cases, very long and very short scales of bathymetric roughness are independent of each other because they may be sculpted by different geomorphic and tectonic processes. For instance, incised canyons on the continental shelf and slope will be independent of the long wavelength structure of the slope itself that is generated, for example, by previous global sea level variations (e.g., Region #15 in Figure 2). Furthermore, the statistical properties of the bathymetry are only approximately constant (i.e., statistically homogeneous) within a particular region and may be different in other locations as a result of different geological processes and age (e.g., abyssal plains vs. continental shelves) (Fox & Hayes, 1985). The analyzed samples of h and ϵ, though, provide evidence of smoothly varying power spectral densities as a function of wavenumber in all samples and a consistent relation between σ_e and σ_m. This is possible because the altimetry-predicted bathymetry, specifically the bathymetry based on the altimetry data used by Tozer et al. (2019), may still contain significant information in the transition from low to high wavenumber content. In the future, as more multibeam surveys become available, the behavior of the power spectral density and the relation between

σ_e and σ_m can be investigated further, refinement of the relation can be carried out, and the limits of the approximation can be established.

The errors in the altimetry-predicted bathymetry, ϵ, are expected to be mainly caused by the absence of high wavenumber content in the original satellite altimetry data. However, some histograms of ϵ in Figure 11b (e.g., Regions #4, #7, #8, and #14) show significant deviations from the Laplacian function and from the histograms of the high wavenumber content of the multibeam data of Figure S4b. Furthermore, the altimetry-predicted bathymetry power spectral amplitudes at low wavenumbers are higher than those of the multibeam data in some regions (see Figure S5). We hypothesize that such deviations are caused by errors within the resolvable waveband of the altimetry-prediction method (i.e., the Inverse Nettleton procedure for $\lambda > 10$ km). The sources of these errors have been extensively investigated. When the seafloor is heavily sedimented, for example, gravity anomalies may reflect the subseafloor basement structure. The predicted bathymetry, therefore, will be erroneously linked to the buried structures rather than the sea floor topography (Smith & Sandwell, 1994). Another relevant source of error is the dependence of water surface heights on steady oceanic currents (Smith, 1998). While the average effect of oceanic currents is usually small as compared to gravity anomalies (45–60 times smaller), nonnegligible effects can be found locally (e.g., at some boundary currents such as the Gulf Stream Smith, 1998). To assess the relative importance of ϵ in the wavenumber domain, Figure S6 presents the relative spectral amplitude errors of ϵ as a function of wavenumber. The relative error spectra are calculated by dividing each spectral bin of the power spectral density of ϵ with that of the multibeam bathymetry (not detrended). The plot shows that errors at low wavenumbers (long wavelengths) are insignificant compared to the actual spectral amplitudes of the bathymetry in the 15 regions.

The statistical models for ϵ, based on a Von Karman covariance function, a Laplacian marginal distribution, and the predictor of σ_e, are sufficiently accurate to assess the uncertainties of tsunami hazard assessments. Simulated tsunamis are insensitive to the differences seen in a and H among the 15 regions. Furthermore, they are insensitive to variations of σ_e within the confidence intervals of the proposed scaling law. However, other type of uncertainty quantification more sensitive to the high wavenumber content (e.g., studies of internal wave dissipation) may require a refinement of the uncertainty model of this study.

The uncertainty model proposed in this paper can be improved by adopting a better random field model and by better understanding the behavior of statistical properties of the seafloor morphology. For instance, the random field model assumed ergodicity, which is somewhat supported for the Chilean analysis. Some regions, though, show significant differences in their local statistics. Thus, we expect that the statistics determined for each specific sample are only valid in the near field and where the processes sculpting the seafloor morphology do not change. Anisotropy can be also included in a future improvement of the random field model. Tectonic processes, for example, produce seafloor structures with preferred orientations, and, consequently, bathymetry may exhibit strong anisotropy at some wavelengths (e.g., see Samples 5 and 7 in Figure 1 and Harper et al., 2019). The study of abyssal hills (Goff et al., 1997; Goff & Arbic, 2010) has also shown that more sophisticated models can be adopted.

6. Conclusions

A great majority of the ocean bathymetry is estimated from satellite altimetry data mapping gravity anomalies at the sea surface. While this technique provides near-complete coverage of the oceans, the approach cannot resolve the high wavenumber content of the bathymetry. By considering the nearly fractal behavior of the bathymetry at high wavenumbers, we propose an isotropic random field model accounting for the uncertainty of altimetry-predicted bathymetry. The random field model is calibrated using the statistical properties of multibeam surveys. We found that for the ocean offshore northern Chile, the marginal distribution of the bathymetry error, ϵ, can be modeled with a Laplacian distribution, and the correlation coefficient function can be modeled with a Von Karman function with average values of $a = 4$ km, $H = 0.975$, and $\sigma_e = 160$ m.

The generation of synthetic bathymetry samples for sensitivity studies is challenging because it should consider that some regions contain data with much lower uncertainty than satellite-predicted data. Consequently, we proposed a conditional random field model to account for areas with and without uncertainty. The conditional fields modeled for the demonstration case in Chile require more than 4,500 K-L terms to obtain variance errors smaller than 20%. We show that the statistics of bathymetry samples converge to

the target probability properties proposed in this study. Because of the high dimensionality of the random field and the large number of grid points required for numerical modeling, the construction of synthetic bathymetry random field samples is challenging in terms of computational demand. To reduce the computational demand, ad-hoc strategies or simplifications should be adopted. For tsunami hazard assessments, for example, bathymetry uncertainties can be disregarded when their standard deviations are much smaller than mean water depths.

The bathymetry uncertainty model and the method for the generation of synthetic bathymetry samples are applied to an illustrative tsunami hazard assessment in northern Chile. The tsunami response is assessed at middle- and near-field offshore and coastal gauges. We demonstrate that leading waves and arrival times at the Chilean coast are not significantly affected by bathymetry uncertainties for near-field tsunami sources. Trailing waves, in contrast, are significantly affected by bathymetry uncertainties. Our study has important implications for tsunami early warning and hazard assessment in Chile employing numerical tsunami models. It demonstrates that altimetry-predicted bathymetry uncertainties do not impact the leading wave amplitude and its arrival time, which are critical parameters to be delivered to coastal communities. This conclusion should be further investigated for other regions and coastal settings and by adopting more sophisticated tsunami propagation models.

As the first step in a broader application of the approach, the analysis was carried out for multibeam data in 15 different globally distributed regions. A systematic study shows that the locally fitted values of a and H have only moderate differences among the regions. These differences are found to be not relevant for tsunami hazard assessments. We determine a set of globally fitted values of $a_g = 6\,\text{km}$ and $H_g = 0.95$. However, the variance σ_e has strong variations among the 15 regions. Hence, we proposed an empirically determined scaling law to predict σ_e at any location, based on the altimetry-predicted bathymetry variance σ_m. These values can serve as a first-order approximation to model bathymetry uncertainties. Several areas of the statistical analysis have been identified for further improvement in terms of the modeled properties. For example, we have assumed that ϵ is isotropic, which may not be adequate everywhere. The ergodicity assumption may also need to be relaxed in future improvements to the uncertainty model.

Acknowledgments
We acknowledge the support of Geomar, who kindly clarified questions about the valuable bathymetry data from their paper, specially H. Kopp and I. Klaucke. I. Sepúlveda would like to acknowledge the support of the John Miles Fellowship and the Cecil and Ida Green Foundation. B. Tozer was supported by the Office of Naval Research (N00014-17-1-2866) and a Cecil and Ida Green Foundation scholarship. J.S. Haase would like to acknowledge the support of National Science Foundation Grant OAC-1835372. P. Liu would like to acknowledge the support through a research grant from the National Research Foundation in Singapore (NRF-NSFC grant) to National University of Singapore. We would like to thank M. Pritchard for helpful ideas during the early stage of this project and D. Sandwell for very insightful discussions about the sources of errors in altimetry-predicted bathymetry and further ideas to improve the statistical analysis. Z. Yin contributed with good ideas to improve the presentation of this paper. J. McGuire also helped on the search of multibeam data sets. We also acknowledge the insightful comments of editors and reviewers, who improved this manuscript significantly.

Data Availability Statement

The SRTM15+V2 is downloaded from https://topex.ucsd.edu. This study also used multibeam bathymetry data provided by Geomar, the Center for Coastal and Ocean Mapping (CCOM) of the Joint Hydrographic Center and Geoscience Australia. The bathymetry data of CCOM are available at https://ccom.unh.edu/data-type/bathymetry. The bathymetry data of Geoscience Australia are available at https://www.ga.gov.au/about/projects/marine/mh370-data-release.

References

An, C., Sepúlveda, I., & Liu, P. L.-F. (2014). Tsunami source and its validation of the 2014 Iquique, Chile, earthquake. *Geophysical Research Letters*, *41*, 3988–3994. https://doi.org/10.1002/2014GL060567

Becker, J., Sandwell, D., Smith, W., Braud, J., Binder, B., Depner, J., et al. (2009). Global bathymetry and elevation data at 30 arc seconds resolution: Srtm30_plus. *Marine Geodesy*, *32*(4), 355–371.

Bell, T. (1975). Statistical features of sea-floor topography. *Deep Sea Research and Oceanographic Abstracts*, *22*, 883–892.

Blakely, R. J. (1996). *Potential theory in gravity and magnetic applications*. Cambridge: Cambridge university press.

Bricker, J. D., Gibson, S., Takagi, H., & Imamura, F. (2015). On the need for larger Manning's roughness coefficients in depth-integrated tsunami inundation models. *Coastal Engineering Journal*, *57*(02), 1550005.

Egbert, G. D., & Ray, R. D. (2001). Estimates of M2 tidal energy dissipation from TOPEX/Poseidon altimeter data. *Journal of Geophysical Research*, *106*(C10), 22,475–22,502.

Fox, C. G., & Hayes, D. E. (1985). Quantitative methods for analyzing the roughness of the seafloor. *Reviews of Geophysics*, *23*(1), 1–48.

Geersen, J., Ranero, C. R., Kopp, H., Behrmann, J. H., Lange, D., Klaucke, I., et al. (2018). Does permanent extensional deformation in lower forearc slopes indicate shallow plate-boundary rupture? *Earth and Planetary Science Letters*, *489*, 17–27.

Gille, S. T., Metzger, E. J., & Tokmakian, R. (2004). Seafloor topography and ocean circulation: Naval Research Lab Stennis Space Center MS Oceanography Division.

Goff, J. A. (1991). A global and regional stochastic analysis of near-ridge abyssal hill morphology. *Journal of Geophysical Research*, *96*(B13), 21,713–21,737.

Goff, J. A. (1993). A utilitarian approach to modeling non-Gaussian characteristics of a topographic field. *Journal of Geophysical Research*, *98*(B11), 19,635–19,647.

Goff, J. A. (2010). Global prediction of abyssal hill root-mean-square heights from small-scale altimetric gravity variability. *Journal of Geophysical Research*, *115*, B12104. https://doi.org/10.1029/2010JB007867

Goff, J. A., & Arbic, B. K. (2010). Global prediction of abyssal hill roughness statistics for use in ocean models from digital maps of paleo-spreading rate, paleo-ridge orientation, and sediment thickness. *Ocean Modelling*, *32*(1–2), 36–43.

Goff, J. A., & Jordan, T. H. (1988). Stochastic modeling of seafloor morphology: Inversion of sea beam data for second-order statistics. *Journal of Geophysical Research*, *93*(B11), 13,589–13,608.

Goff, J. A., Ma, Y., Shah, A., Cochran, J. R., & Sempéré, J.-C. (1997). Stochastic analysis of seafloor morphology on the flank of the Southeast Indian ridge: The influence of ridge morphology on the formation of abyssal hills. *Journal of Geophysical Research*, *102*(B7), 15,521–15,534.

Grigoriu, M. (1995). Applied non-gaussian processes: Examples, theory, simulation, linear random vibration, and MATLAB solutions(Book). Englewood Cliffs, NJ: Prentice Hall, Inc, 1995.

Grigoriu, M. (2012). *Stochastic systems: Uncertainty quantification and propagation*. London: Springer Science & Business Media.

Harper, H., Tozer, B., Parnell-Turner, R., & Sandwell, D. T. (2019). The morphology and tectonic interpretation of "See-saw" Propagators. AGUFM, 2019, T43F-0518.

Hu, Q., Huang, X., Zhang, Z., Zhang, X., Xu, X., Sun, H., et al. (2020). Cascade of internal wave energy catalyzed by eddy-topography interactions in the deep South China Sea. *Geophysical Research Letters*, *47*, e2019GL086510. https://doi.org/10.1029/2019GL086510

Kelker, D. (1970). Distribution theory of spherical distributions and a location-scale parameter generalization. *Sankhyā: The Indian Journal of Statistics Series A*, *32*, 419–430.

Kopp, H., Lange, D., Hannemann, K., Krabbenhoeft, A., Petersen, F., & Timmermann, A. (2016). RV SONNE Fahrtbericht/Cruise Report so244/2. GeoSEA: Geodetic Earthquake Observatory on the Seafloor, Antofagasta (Chile)—Antofagasta (Chile), 27.11.-13.12. 2015.

Kunze, E., & Smith, S. G. L. (2004). The role of small-scale topography in turbulent mixing of the global ocean. *Oceanography*, *17*(1), 55–64.

Liu, X., & Guillas, S. (2017). Dimension reduction for Gaussian process emulation: An application to the influence of bathymetry on tsunami heights. *SIAM/ASA Journal on Uncertainty Quantification*, *5*(1), 787–812.

Mandelbrot, B. B. (1967). How long is the coast of Britain. *Science*, *156*(3775), 636–638.

Mayer, L., Jakobsson, M., Allen, G., Dorschel, B., Falconer, R., Ferrini, V., et al. (2018). The Nippon Foundation—GEBCO Seabed 2030 Project: The quest to see the world's oceans completely mapped by 2030. *Geosciences*, *8*(2), 63.

Mofjeld, H. O., Titov, V. V., González, F. I., & Newman, J. C. (2001). Tsunami scattering provinces in the Pacific Ocean. *Geophysical Research Letters*, *28*(2), 335–337.

SHOA (2009). Atlas hidrografico de la Armada de Chile, 7th edition.

Sepúlveda, I., Liu, P. L.-F., Grigoriu, M., & Pritchard, M. (2017). Tsunami hazard assessments with consideration of uncertain earthquake slip distribution and location. *Journal of Geophysical Research: Solid Earth*, *122*, 7252–7271. https://doi.org/10.1002/2017JB014430

Smith, W. H. F. (1998). Seafloor tectonic fabric from satellite altimetry. *Annual Review of Earth and Planetary Sciences*, *26*(1), 697–747.

Smith, W. H. F., & Sandwell, D. T. (1994). Bathymetric prediction from dense satellite altimetry and sparse shipboard bathymetry. *Journal of Geophysical Research*, *99*(B11), 21,803–21,824.

Smith, W. H. F., & Sandwell, D. T. (1997). Global sea floor topography from satellite altimetry and ship depth soundings. *Science*, *277*(5334), 1956–1962.

Timko, P. G., Arbic, B. K., Goff, J. A., Ansong, J. K., Smith, W. H. F., Melet, A., & Wallcraft, A. J. (2017). Impact of synthetic abyssal hill roughness on resolved motions in numerical global ocean tide models. *Ocean Modelling*, *112*, 1–16.

Titov, V. V., & Gonzalez, F. (1997). Implementation and testing of the Method of Splitting Tsunami (MOST) model. US Department of Commerce, National Oceanic and Atmospheric Administration, Environmental Research Laboratories, Pacific Marine Environmental Laboratory.

Tozer, B., Sandwell, D. T., Smith, W. H. F., Olson, C., Beale, J. R., & Wessel, P. (2019). Global bathymetry and topography at 15 arc sec: SRTM15+. *Earth and Space Science*, *6*, 1847–1864. https://doi.org/10.1029/2019EA000658

Wang, X. (2009). User manual for COMCOT version 1.7 (first draft). Cornell University.

Weatherall, P., Marks, K., Jakobsson, M., Schmitt, T., Tani, S., Arndt, J. E., et al. (2015). A new digital bathymetric model of the world's oceans. *Earth and Space Science*, *2*, 331–345. https://doi.org/10.1002/2015EA000107

Williams, C. N., Cornford, S. L., Jordan, T. M., Dowdeswell, J. A., Siegert, M. J., Clark, C. D., et al. (2017). Generating synthetic fjord bathymetry for coastal Greenland. *Cryosphere Discussions*, *11*, 363–380.